ORNL/TM-2023/2919

Mechanical Properties of Additively Manufactured 316L Stainless Steel Before and After Neutron Irradiation–FY23

T. S. Byun
A. G. Le Coq
J. W. Werden
T. G. Lach
K. D. Linton

May 2023

M3CT-23OR1305081

OAK RIDGE National Laboratory

ORNL IS MANAGED BY UT-BATTELLE LLC FOR THE US DEPARTMENT OF ENERGY

ORNL/TM-2023/2919

Advanced Materials and Manufacturing Technologies Program

MECHANICAL PROPERTIES OF ADDITIVELY MANUFACTURED 316L STAINLESS STEEL BEFORE AND AFTER NEUTRON IRRADIATION–FY23

T. S. Byun
A. G. Le Coq
J. W. Werden
T. G. Lach
K. D. Linton

May 2023

M3CT-23OR1305081

Prepared by
OAK RIDGE NATIONAL LABORATORY
Oak Ridge, TN 37831-6283
managed by
UT-BATTELLE, LLC
for the
US DEPARTMENT OF ENERGY
under contract DE-AC05-00OR22725

CONTENTS

LIST OF FIGURES

LIST OF TABLES

ACKNOWLEDGEME**NTS**

This research was sponsored by the US Department of Energy Office of Nuclear Energy's Advanced Materials and Manufacturing Program under contract DE-AC05-00OR22725 with UT-Battelle LLC. The authors thank David Collins and Stephen Taller for their thoughtful review of this report before publication.

Mechanical Properties of Additively Manufactured 316L Stainless Steel Before and After Neutron Irradiation–FY23

T.S. Byun, J.W. Werden, A.G. Le Coq, T.G. Lach, K.D. Linton

ABSTRACT

This report presents the observed mechanical behavior of the additively manufactured (AM) 316L stainless steel (SS) before and after neutron irradiation. In the Advanced Materials and Manufacturing Technologies (AMMT) program, a variety of mechanical and physical property data are generated and accumulated to assess the AM austenitic alloy for nuclear reactor applications. The testing and evaluation task in the FY 2023 focused on elucidating the effects of sampling location and build size on the mechanical properties of AM 316L SS (in stress-relieved condition) before and after neutron irradiation. The laser powder bed fusion (LPBF) process produced 316L plates of three distinct sizes from which SS-J3 miniature tensile specimens were machined from six different locations. The tensile specimens were irradiated in the High Flux Isotope Reactor (HFIR) normally to 2 and 10 dpa at the target temperatures of 300 °C and 600 °C. Post-irradiation tensile testing was performed at room temperature, 300 °C, and 600 °C. The mechanical properties of AM 316L SS were significantly influenced by the characteristic microstructures of printed materials, which include fine grains and high-density dislocations. Compared with the traditional 316L SS, AM 316L showed higher initial strength and lower ductility. Regardless of sampling location, the AM 316L steel retained relatively high strength and ductility to the highest irradiation dose. A prompt necking at yield (with little uniform ductility) was observed after irradiation at 300 °C but no embrittlement was observed up to 10 dpa. Ductilization by irradiation–the radiation-induced increase of ductility–was observed for the 600 °C irradiation only and it occurred in low dose range only. The neutron irradiation increased the data variation in many tensile property datasets, particularly after 600 °C irradiation, and no clear dependence of tensile properties on build thickness or sampling location was observed.

1. INTRODUCTION

Reactor core materials in advanced nuclear energy systems will be subject to high-temperature and high-dose neutron irradiations, which will significantly change the microstructures and local chemistries of the materials and thus degrade their mechanical, chemical, and physical properties [1]. Therefore, the core materials for any high-performance reactor will require excellent high-temperature mechanical properties, high-radiation resistance, and high-corrosion resistance, in addition to the feasibility of manufacturing processes. The 300 series SSs are widely used in the reactor core and coolant system components of current nuclear power plants and have been among the key candidate structural materials for advanced future reactors, including sodium-cooled fast reactors and fusion energy systems [2-6]. Austenitic alloys have been used consistently for nuclear applications because they provide a good combination of strength, ductility, toughness, and oxidation-corrosion resistance over an exceptionally wide temperature range [7]. Their austenitic (i.e., face-centered cubic) structure is highly stable within and beyond the possible reactor operation temperature ranges, which should enable these alloys to retain such good properties in reactor environments [2,4,5,7]. In particular, their high phase stability, high ductility, and toughness lead to excellent resistance to radiation damage and embrittlement during in-reactor service [2,7].

Additive manufacturing technologies will provide many opportunities and challenges if they are used to build a nuclear reactor core. These technologies offer enormous flexibility in designing and building complex components that can be cost prohibitive with traditional manufacturing methods. Indeed, recent research efforts confirmed that austenitic SSs are highly suitable for additive manufacturing of complex shaped reactor components [8-11]. This suitability is likely due to the fast cooling that occurs during the AM process, preventing the formation of the high-temperature ferrite (i.e., δ-ferrite) phase during cooling, which is metastable and undergoes degradation at high temperatures caused by phase decomposition and segregation. The high oxidation resistance [7] might help form relatively clean boundaries between printed layers. Multiple AM technologies have advanced rapidly in recent years and are now poised to revolutionize the design and manufacture of complex components in a fully computerized manner [9]. Examples of such key AM technologies that are deemed relevant to nuclear reactor core structures include the LPBF process via selective laser melting or electron beam melting, laser-directed energy deposition, and binder jetting combined with a chemical vapor infiltration process for ceramics [8].

In principle, the microstructures–and thus the mechanical properties–of AM alloys can be tailored by changing processing parameters, such as scan speed, laser power, powder feedstock purity, and powder layer thickness [12-14]. In particular, the size and orientation of the fine-grained dislocation cell structure in metallic materials can be easily controlled by changing processing parameters [10,15-17] or applying post-build heat treatments [13]. Although an optimized LPBF process can produce a very fine and desirable metastable microstructure owing to the fast cooling and solidification, many unknowns and adverse effects remain regarding the microstructural and chemical stability of AM materials in high-temperature, corrosion, and irradiation environments. The as-printed materials displayed increased room temperature yield strength (YS) but less work hardening because of a characteristic microstructure of fine grains and dislocation cells formed during the localized rapid solidification [15,18-20]. Recent test results indicate that these fine-grained structures with mobile dislocations can shorten the high-temperature creep life [8,10,21]. Furthermore, the fracture toughness of AM 316L SS could be negatively affected by the increased porosity from the build process, structural anisotropy relative to the build direction, and inclusions from impurities in the feedstock powder [12,22]. Neutron or ion irradiation could also significantly affect the behaviors (i.e., shortened creep life and reduced fracture toughness) observed in AM alloys [11,23-25].

To ensure successful reactor core design using AM components, assessing the materials performance and structural integrity of AM components is essential. Therefore, the AMMT program has a long-term testing and evaluation plan to accumulate materials properties data before and after irradiation and build a

materials property handbook for reactor application of the AM 316L steels, which is also a continuing task from the former Transformational Challenge Reactor (TCR) program. In addition to the initial characterization of AM 316L and wrought (WT) 316L steels, two irradiation and post-irradiation examination (PIE) campaigns have been performed to evaluate the tensile deformation and failure properties of the AM 316L SSs before and after irradiation. The Campaign-1 focused on the effects of radiation on the mechanical properties and microstructure of the 316L SSs in different conditions (i.e., as-built, stress-relieved, and fully-annealed conditions and traditional wrought condition) [26]. This report presents the baseline and PIE results of the Campaign-2, which was intended to elucidate the effects of sampling location and build size on the mechanical properties before and after irradiation.

2. PROGRESS IN THE PAST YEARS

In the earlier Campaign-1 (2019-2020), AM 316L steels were characterized in three different conditions: as-built, stress-relieved (650°C/1 h), and solution-annealed (1,050°C/1 h) conditions. The reference wrought (WT) 316L alloy in the solution-annealed condition underwent the same tests for comparison. Baseline testing included uniaxial tensile testing at various temperatures and in situ deformation and failure testing in scanning electron microscopy (SEM). PIE for the 316L alloy in all four material conditions included static tensile testing at 25 °C–600 °C. An earlier report [10] analyzed the key mechanical property data for the AM 316L SS samples produced by the TCR program. This report's analysis focuses on the baseline tensile characteristics, the effect of post-build heat treatments, and the effect of radiation on tensile deformation behaviors for the 316L SS samples in the four different conditions. Furthermore, the statistical and spatial distribution behaviors of mechanical properties and unique microstructural characteristics are also discussed in detail.

The irradiation experiment and PIE efforts for assessing metallic materials focused on evaluating the mechanical performance of AM components over the reactor-relevant temperature range. Thus far, the two irradiation and PIE campaigns for metallic materials have been completed: 14 rabbit capsules containing SS-J2 and SS-J3 tensile specimens (6 and 8 rabbit capsules, respectively, for the Campaign-1 and Campaign-2) were irradiated at target temperatures of 300 and 600 °C up to 10 dpa in the HFIR located at the US DOE's Oak Ridge National Laboratory (ORNL).

The tensile testing results before and after HFIR irradiation are compared in the Campaign-1 PIE report [26] and are summarized as follows: Regardless of the postbuild processing, the AM 316L SS before irradiation showed higher strength but relatively similar ductility compared with the reference 316L SS. Both the strength and the ductility of AM 316L and WT 316L SSs decreased with the test temperature. A significant effect of postbuild heat treatment was measured mostly in the low-strain region, and the effect became much smaller in the later part of deformation. Weibull plots of tensile property data indicated that in general larger variability was found in the ductility datasets than in the strength datasets. The tensile properties for the specimen set from various build locations showed clear location dependence, although the measured variations were insignificant. Overall, the AM 316L SS demonstrated high strength and high ductility regardless of different post-build heat treatments and significant variations in datasets.

Neutron irradiation induced significant changes in the mechanical behavior of AM SSs, including radiation-induced hardening and softening. Irradiation hardening was generally lower in the relatively stronger materials (i.e., the as-built and stress-relieved AM SSs) than in the solution-annealed AM and WT SSs. Relatively lower strength 316L SS retained better ductility, regardless of irradiation conditions; however, the stronger 316L SS demonstrated similar levels of ductility after the higher temperature (~600°C) irradiation. The as-built 316L SS after irradiation at 300°C showed unstable plastic deformation (i.e., necking) immediately after yielding, whereas the tensile property changes under other irradiation conditions were much less significant. No embrittlement (i.e., failure before yielding) was observed

within the tensile test campaign or in the irradiation conditions explored in the experiment, which could serve as the basis for assessing the AM 316L SS for in-reactor applications.

As a special phenomenon for high strength materials, the irradiation-induced ductilization behavior was observed after the higher temperature irradiation. Dynamic strain aging was also observed in the stress-strain curves obtained at high temperatures (≳400°C), regardless of irradiation dose; however, any detrimental effects are insignificant. Based on the baseline and postirradiation test results obtained so far, the stress-relieved AM 316L is considered the standard condition of AM 316L for the AMMT program evaluation because it retains high strength without showing any risk of embrittlement (i.e., a complete loss of ductility) during service.

3. EXPERIMENTAL

3.1 Materials and Specimens

The material tested before and after irradiation for Campaign-2 is the 316L SS additively manufactured using the LPBF method. The base material used for printing was 15–45 μm powder feedstock from Praxair, the nominal composition of which is listed in Table 1.

Table 1. Chemical composition of AM 316L (Praxair) powder (wt.%)

Materials	Fe	Cr	Ni	Mo	Mn	Si	N	Cu	Co	C	P	O
AM 316L (Praxair powder)	Bal.	17.01	12.67	2.48	1.29	0.59	0.01	0.00	0.08	<0.005	<0.005	0.03

Thin (1 mm) and thick (5 mm) plates and 40 mm thick cubes were printed in an Ar gas environment in the Concept Laser M2, a GE AM system. The build identification number was 20201119, which is identical with the printing date. Typical or vendor-recommended processing parameters were used for the build: 370 W laser power, 1,350 mm/s scan speed, 130 μm beam size, 90 μm hatch spacing, and 50 μm layer thickness. SS-J3 (small specimen-Japanese type, 30 mil thick) specimens were machined using electrical discharge machining (EDM) from various locations of the as-built plates and cubes, Figure 1.

The SS-J3 specimen has a 1.2 mm wide, 0.75 mm thick, and 5 mm long gage section with a total length of 16 mm and a head width of 4 mm. The as-built pieces were sliced into nominally 0.75 mm thin sheets and about 240 specimens were machined from the sheets sliced from 6 different locations of the build pieces: (1) 1.5 mm thick block layers, (2) 5 mm thick block center layers, (3) 5 mm thick block surface layers, (4) 40 mm cube center layers, (5) 40 mm cube 10 mm from edge, (6) 40 mm cube surface layers. An example of the as-EDMed specimens is shown in Figure 2, where the specimens are still connected via small ligaments that are broken and ground off later. The specimen length coincides with the build (*Z*) direction corresponding to the growth (i.e., layer stacking) direction in the LPBF process.

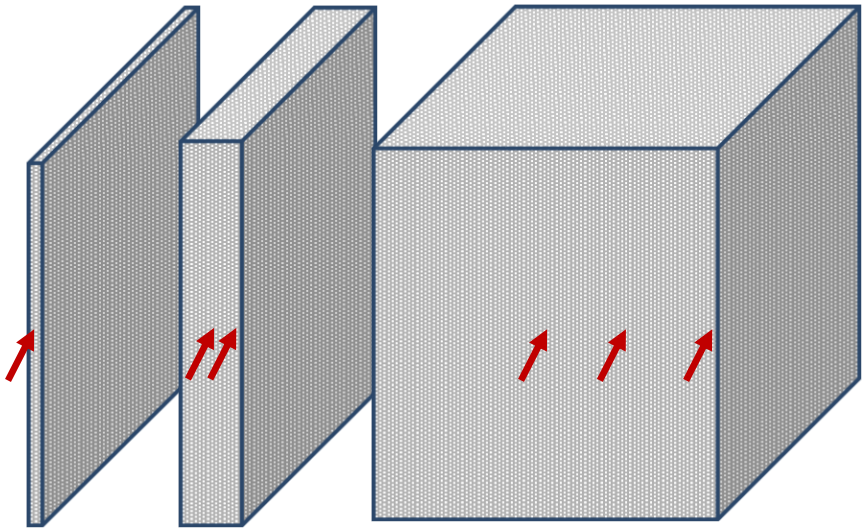

Figure 1. Schematic of the build blocks showing the sampling locations

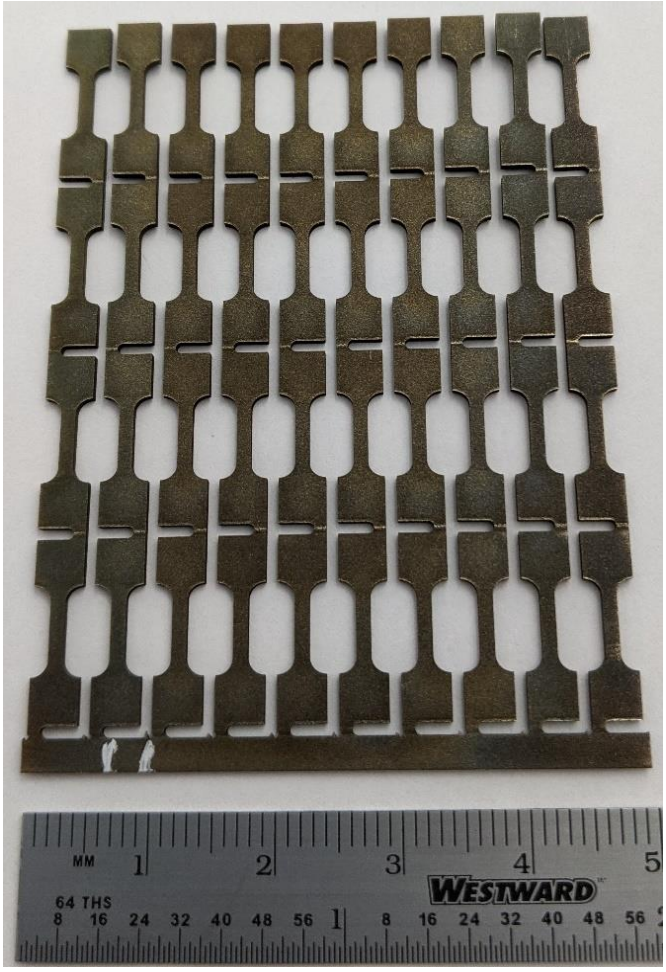

Figure 2. Specimen array after EDM cutting of a sheet sliced from a 5 mm thick as-built plate.

Figure 3 displays an example set of rabbit capsule contents (displayed for capsule GTCR07) including 24 SS-J3 tensile specimens and 12 thermometry specimens (SiC coupons). The capsule type used for containing these contents is the GENTEN capsule design, which is standardized for the SS-J2 and J3 miniature tensile specimens [27,28].

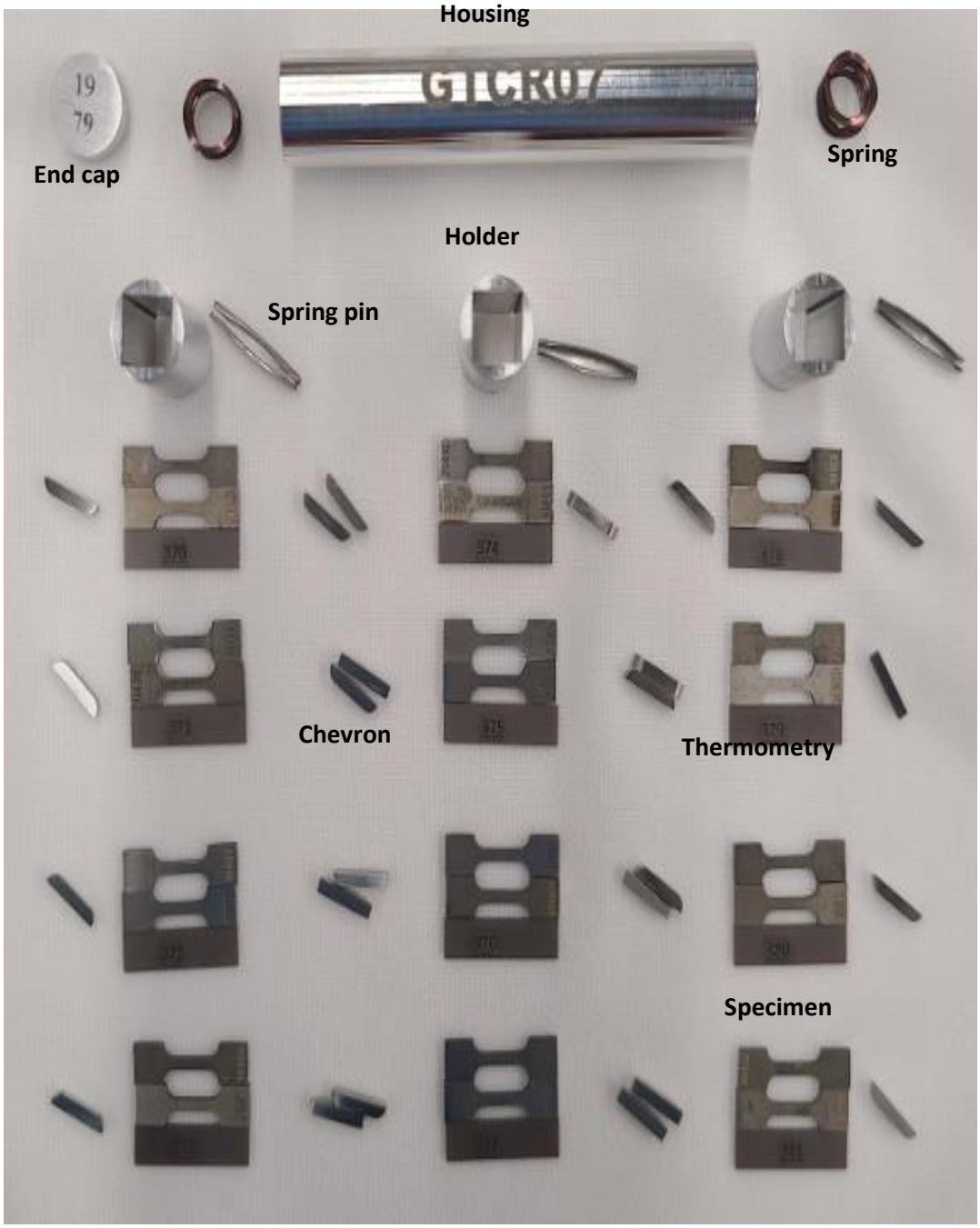

Figure 3. A set of tensile specimens and capsule components to be assembled into one rabbit capsule. Shown is the capsule GTRC07 for the irradiation of AM 316L.

3.2 Irradiation Experiment and PIE Status

In the AMMT (and former TCR) program, multiple irradiation and PIE campaigns have been performed to produce materials performance data for assessing the AM metallic materials. The irradiation and PIE campaigns for 316L SS include irradiating 14 rabbit capsules in HFIR. This report presents and discusses the PIE results for the AM 316L specimens irradiated in the GTCR07 through GTCR10 capsules under Campaign-2. This campaign was designed specifically for elucidating the effects of sampling locations on mechanical properties and microstructure changes.

This section details the status of the irradiation-PIE campaigns. Key information for the completed irradiation campaigns is summarized in Table 2, which includes the target irradiation temperatures and doses of the 14 rabbit capsules and the tensile specimens loaded into these capsules. The two irradiation campaigns performed in FY2020 and FY2022 intended to test three different aspects and materials:

(1) The first six capsules (FY2020) tested radiation effects on the AM 316L alloy in three different conditions (i.e., as-built, stress-relieved, and solution-annealed) and on the WT 316L reference alloy. Most of the PIE results from the 0.2 and 2 dpa capsules (GTCR01, GTCR02, GTCR04, and GTCR05) and the baseline test data for corresponding conditions were presented in the previous report [26]. PIE for the specimens irradiated to 10 dpa (from GTCR03 and GTCR06) is currently under preparation because the irradiation of those capsules was completed. Microscopy effort also has been exerted, and the results are expected to be available in the next milestone report.

(2) The next four capsules (GTCR07–GTCR10 for FY2021–FY2022) include the AM 316L specimens taken from six different locations of 3D printed plates and cubes (Figure 1), which will test the effect of depth from the surfaces of 3D printed components. Because the baseline testing in FY19 and the irradiation and PIE for FY2020–FY2021 led to the conclusion that AM 316L can perform best in the stress-relieved condition, the AM 316L specimens in this condition are irradiated in the ongoing and future irradiation campaigns.

(3) The last four capsules (GTCR11–GTCR14 for FY2021) are for the AM alloy 718 in four different heat-treatment conditions, which are the standard WT alloy 718 (i.e., solution-annealed and γ'- and γ''-aged conditions) and the AM alloy 718 in three different conditions (i.e., standard condition, solution-annealed condition, and solution-annealed at lowered temperature, as well as the γ'- and γ''-aged conditions). Additional AM 316L specimens from different build locations are loaded in the spare spaces in these capsules. The PIE results for the alloy 718 have been reported in a separate report [29].

Table 2. Irradiation effect research and tensile specimens for metallic materials

FY	Capsule ID	Irr. Temp. (°C) Target/Measured	Dose (dpa)	Specimen/alloy
2020	GTCR01	300/250	0.2	36 SS-J2 (AM 316L in as-built, stress-relieved, and solution-annealed conditions and WT 316L)
	GTCR02	300/376	2	36 SS-J2 (AM 316L in as-built, stress-relieved, and solution-annealed conditions and WT 316L)
	GTCR03	300/277	10	36 SS-J2 (AM 316L in as-built, stress-relieved, and solution-annealed conditions and WT 316L)
	GTCR04	600/673	0.2	36 SS-J2 (AM 316L in as-built, stress-relieved, and solution-annealed conditions and WT 316L)
	GTCR05	600/600	2	36 SS-J2 (AM 316L in as-built, stress-relieved, and solution-annealed conditions and WT 316L)
	GTCR06	600/550	10	36 SS-J2 (AM 316L in as-built, stress-relieved, and solution-annealed conditions and WT 316L)
2021-2022	GTCR07	300/292	2	24 SS-J3 (AM 316L in stress-relieved condition, sampling from six build locations of 1.5 mm and 5 mm thick plates and 40 mm cube)
	GTCR08	600/494	2	24 SS-J3 (AM 316L in stress-relieved condition, sampling from six build locations of 1.5 mm and 5 mm thick plates and 40 mm cube)
	GTCR09	300/269	10	24 SS-J3 (AM 316L in stress-relieved condition, sampling from six build locations of 1.5 mm and 5 mm thick plates and 40 mm cube)
	GTCR10	600/511	10	24 SS-J3 (AM 316L in stress-relieved condition, sampling from six build locations of 1.5 mm and 5 mm thick plates and 40 mm cube)
	GTCR11	300/305	2	24 SS-J2 (WT IN 718 in standard, one solution-annealed, and two age-hardened conditions, AM IN 718) and 8 SS-J3 (AM 316L in stress-relieved condition, six build locations)
	GTCR12	600/553	2	24 SS-J2 (WT IN 718 in standard, one solution-annealed, and two age-hardened conditions, AM IN 718) and 8 SS-J3 (AM 316L in stress-relieved condition, six build locations)
	GTCR13	300/318	10	24 SS-J2 (WT IN 718 in standard, one solution-annealed, and two age-hardened conditions, AM IN 718) and 8 SS-J3 (AM 316L in stress-relieved condition, six build locations)
	GTCR14	600/578	10	24 SS-J2 (WT IN 718 in standard, one solution-annealed, and two age-hardened conditions, AM IN 718) and 8 SS-J3 (AM 316L in stress-relieved condition, six build locations)

3.3 Mechanical Testing at Irradiated Materials Examination and Testing Facility

Uniaxial tensile testing for SS-J3 specimens was performed by using the static Instron-5kN system at the Irradiated Materials Examination and Testing facility. Ninety tension tests were performed at a nominal strain rate of 5×10^{-4} s^{-1} (displacement rate = 0.15 mm/min) by using shoulder loading grip sets [30]. Raw data or load-displacement data up to failure were recorded and used to determine the common engineering strength and ductility parameters, including YS, ultimate tensile strength (UTS), uniform elongation (UE), and total elongation (TE). If not specified otherwise, tensile testing and data analysis were performed by following the standard testing procedure in ASTM E8/8M and E21 [31,32]. Tables 3–5 list the irradiated and non-irradiated SS-J2 tensile specimens tested at room temperature, 300 °C and 600 °C, respectively. The high cost and time for handling highly radioactive specimens limited the number of tests for the irradiated materials. Therefore, one test was performed per irradiation and test condition.

Table 3. Tensile test matrix for the irradiated and nonirradiated SS-J3 specimens tested at room temperature

Capsule ID	Target Irradiation Temp. (°C)	Dose (dpa)	Sampling Location	Specimen ID	Test Temp. (°C)
Control	–	0	1.5mm plate layer	14016	25
Control	–	0	40mm cube 10mm from surface	11161	25
Control	–	0	40mm cube center layer	11138	25
Control	–	0	40mm cube surface layer	21006	25
Control	–	0	5mm block center layer	13028	25
Control	–	0	5mm block surface layer	13081	25
GTCR07	300	2	1.5mm plate layer	22014	25
GTCR07	300	2	40mm cube 10mm from surface	11428	25
GTCR07	300	2	40mm cube center layer	21089	25
GTCR07	300	2	40mm cube surface layer	11555	25
GTCR07	300	2	5mm block center layer	13133	25
GTCR07	300	2	5mm block surface layer	19087	25
GTCR09	300	10	1.5mm plate layer	32001	25
GTCR09	300	10	40mm cube 10mm from surface	11437	25
GTCR09	300	10	40mm cube center layer	21364	25
GTCR09	300	10	40mm cube surface layer	21571	25
GTCR09	300	10	5mm block center layer	13048	25
GTCR09	300	10	5mm block surface layer	30015	25
GTCR08	600	2	1.5mm plate layer	22020	25
GTCR08	600	2	40mm cube 10mm from surface	11554	25
GTCR08	600	2	40mm cube center layer	11069	25
GTCR08	600	2	40mm cube surface layer	21048	25
GTCR08	600	2	5mm block center layer	19021	25
GTCR08	600	2	5mm block surface layer	30038	25
GTCR10	600	10	1.5mm plate layer	14020	25
GTCR10	600	10	40mm cube 10mm from surface	21239	25
GTCR10	600	10	40mm cube center layer	21501	25
GTCR10	600	10	40mm cube surface layer	11336	25
GTCR10	600	10	5mm block center layer	13158	25
GTCR10	600	10	5mm block surface layer	19186	25

Table 4. Tensile test matrix for the irradiated and nonirradiated SS-J3 specimens tested at 300 °C

Capsule ID	Target Irradiation Temp. (°C)	Dose (dpa)	Sampling Location	Specimen ID	Test Temp. (°C)
Control	–	0	1.5mm plate layer	22023	300
Control	–	0	40mm cube 10mm from surface	11239	300
Control	–	0	40mm cube center layer	11171	300
Control	–	0	40mm cube surface layer	21065	300
Control	–	0	5mm block center layer	13033	300
Control	–	0	5mm block surface layer	13096	300
GTCR07	300	2	1.5mm plate layer	14001	300
GTCR07	300	2	40mm cube 10mm from surface	21416	300
GTCR07	300	2	40mm cube center layer	21357	300
GTCR07	300	2	40mm cube surface layer	11241	300
GTCR07	300	2	5mm block center layer	13003	300
GTCR07	300	2	5mm block surface layer	13091	300
GTCR09	300	10	1.5mm plate layer	32020	300
GTCR09	300	10	40mm cube 10mm from surface	11311	300
GTCR09	300	10	40mm cube center layer	21159	300
GTCR09	300	10	40mm cube surface layer	11322	300
GTCR09	300	10	5mm block center layer	30026	300
GTCR09	300	10	5mm block surface layer	30034	300
GTCR08	600	2	1.5mm plate layer	32021	300
GTCR08	600	2	40mm cube 10mm from surface	21311	300
GTCR08	600	2	40mm cube center layer	21069	300
GTCR08	600	2	40mm cube surface layer	21564	300
GTCR08	600	2	5mm block center layer	19080	300
GTCR08	600	2	5mm block surface layer	13046	300
GTCR10	600	10	1.5mm plate layer	32013	300
GTCR10	600	10	40mm cube 10mm from surface	21266	300
GTCR10	600	10	40mm cube center layer	11406	300
GTCR10	600	10	40mm cube surface layer	11294	300
GTCR10	600	10	5mm block center layer	19180	300
GTCR10	600	10	5mm block surface layer	19039	300

Table 5. Tensile test matrix for the irradiated and nonirradiated SS-J3 specimens tested at 600 °C

Capsule ID	Target Irradiation Temp. (°C)	Dose (dpa)	Sampling Location	Specimen ID	Test Temp. (°C)
Control	–	0	1.5mm plate layer	27020	600
Control	–	0	40mm cube 10mm from surface	11355	600
Control	–	0	40mm cube center layer	11200	600
Control	–	0	40mm cube surface layer	21204	600
Control	–	0	5mm block center layer	13043	600
Control	–	0	5mm block surface layer	19034	600
GTCR08	600	2	1.5mm plate layer	14015	600
GTCR08	600	2	40mm cube 10mm from surface	21182	600
GTCR08	600	2	40mm cube center layer	21192	600
GTCR08	600	2	40mm cube surface layer	11301	600
GTCR08	600	2	5mm block center layer	19125	600
GTCR08	600	2	5mm block surface layer	19088	600
GTCR10	600	10	1.5mm plate layer	14022	600
GTCR10	600	10	40mm cube 10mm from surface	11023	600
GTCR10	600	10	40mm cube center layer	11426	600
GTCR10	600	10	40mm cube surface layer	21255	600
GTCR10	600	10	5mm block center layer	19174	600
GTCR10	600	10	5mm block surface layer	19089	600

4. RESULTS AND DISCUSSION

The following four sections cover the radiation effects on the mechanical performance of AM 316L steels, focusing on two topics: (i) the dependencies of the engineering tensile parameters on test temperature, irradiation dose, and temperature (Sections 4.1 and 4.2) and (ii) the effect of different sampling locations on the tensile properties before and after irradiation (Sections 4.3 and 4.4). In all tensile property vs. dose plots, a six-component dataset from the six different sampling locations is presented for each set of testing and irradiation conditions and the variation in each six-component dataset is discussed in the latter two sections. For the purposes of this discussion, the temperatures are discussed broadly in terms of the planned and designed irradiation temperature rather than the measured temperatures presented in Table 3.

The engineering stress–strain curves were produced from the raw data (i.e., load-displacement data) files and are presented in Appendix A. Although the engineering parameters are used in the following sections to describe and highlight the findings regarding the topics (i) and (ii) above, more direct comparisons among the stress–strain curves from different sampling locations are provided in Appendix A.

4.1 Dependence of Strength on Irradiation Dose and Temperature

Because the YS is determined at a very small strain (0.2 % plastic strain), it usually represents the strength of a material in early plastic deformation and should be highly sensitive to the defect density and distribution of the microstructure before deformation. One of the most influential factors in YS change is the irradiation temperature because it determines the degree of defect annihilation during irradiation and thus the density and size of surviving defects in the as-irradiated microstructures [33]. As shown in Figure 4, the dose dependencies of YS at room temperature after the lower temperature (300 °C) irradiation and higher temperature (600 °C) irradiation are starkly different: the YS after 300 °C irradiation increased by > 50% at 2 dpa and by > 200% at 10 dpa, whereas the 600 °C irradiation caused little irradiation hardening or even slight decrease of YS. In the YS data measured at 300 °C (Figure 5), the dose dependence is very similar to that of the room temperature data although the YS values are lower (~300 MPa versus ~390 MPa before irradiation).

The percent increases of YS after the 600°C irradiation are higher: >200% hardening at 2 dpa and >300% hardening at 10 dpa. Figure 6 also indicates that the YS data measured at 600°C, which are displayed only for the 600°C irradiation, show slight decrease or little change after irradiation. Therefore, defect generation and annihilation rates are nearly balanced during irradiation at 600°C, whereas defect survival is much stronger during the lower temperature (300°C) irradiation, and thus defects are accumulating at least up to 10 dpa.

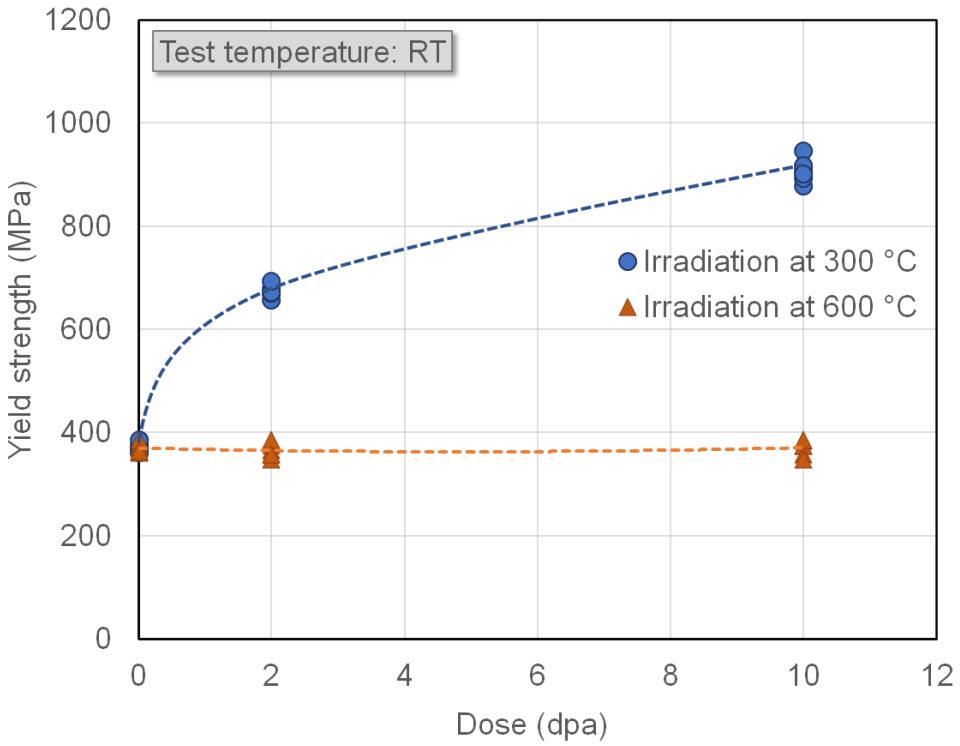

Figure 4. Effect of neutron irradiation on yield strength at room temperature (note: each data clusters have six data points)

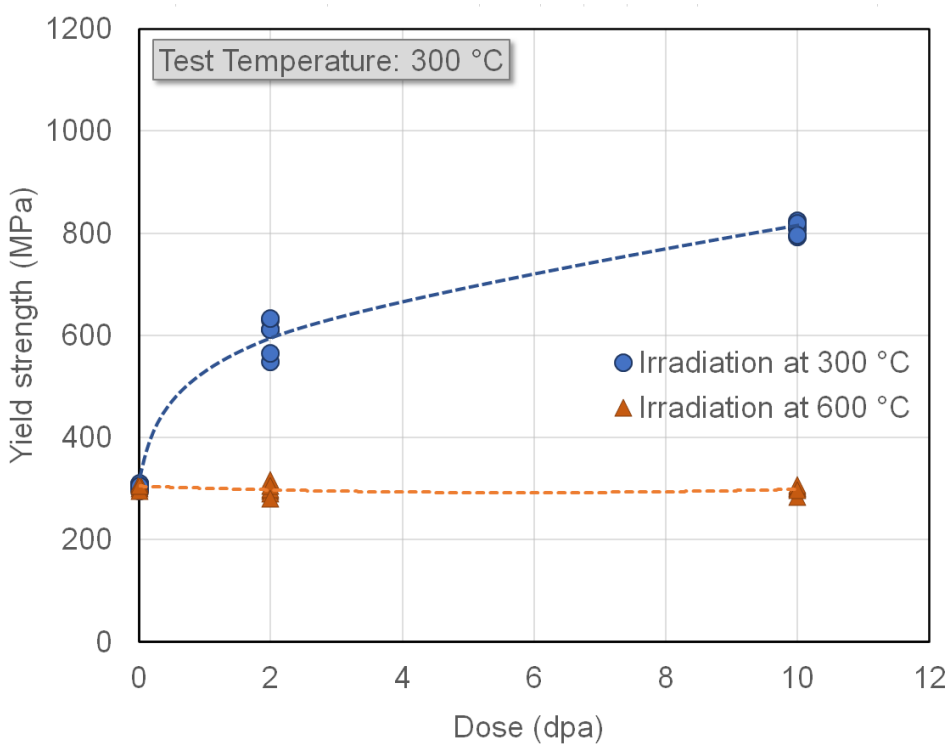

Figure 5. Effect of neutron irradiation on yield strength at 300 °C

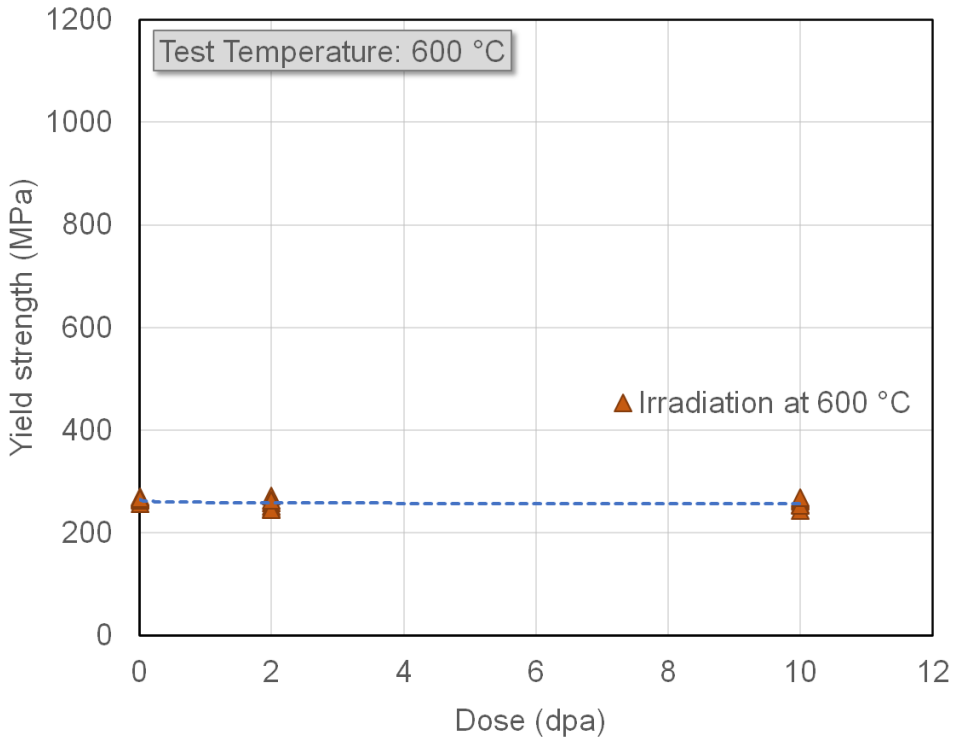

Figure 6. Effect of neutron irradiation on yield strength at 600 °C

In the ductile materials such as the SSs, the UTS is measured after the specimen experiences significant uniform plasticity or at the onset of localization or necking. Therefore, the UTS data usually represents the strength of a material at a significant plastic strain when the specimen is at a maximum load-bearing capability. A high strength alloy usually shows relatively low work hardening capability during deformation, and some small radiation induced defects can be erased by dislocations. This behavior is confirmed by the observation that UTS is less sensitive to the density and distribution of radiation induced defects and thus to its dose when compared with the YS behavior. Indeed, both Figure 7 and Figure 8 show that the dose dependencies of UTS at room temperature and at 300 °C after the lower temperature (300 °C) irradiation are more moderate than those of YS: the UTS after 300 °C irradiation increased by > 30% at 2 dpa and by > 60–90% at 10 dpa. After higher temperature (600 °C) irradiation the dose dependence of UTS is still significantly different from that after the lower temperature irradiation. However, the 600 °C irradiation caused a weak irradiation hardening, which is measured by a 15%–20% increase in UTS at 10 dpa. As observed in Figure 6, Figure 9 shows that the UTS data measured at 600 °C after 600 °C irradiation show little change over the tested dose range.

Interestingly, the UTS values at 600 °C after 600 °C irradiation show significant scattering within the six-component dataset. Such variation is much smaller in the UTS datasets after 300 °C irradiation and in the YS datasets in any irradiation conditions. Because a more rigorous microstructure evolution is expected during irradiation at a high temperature than at a low temperature, the larger scattering at the highest dose of 10 dpa should indicate that it is not caused by different sampling locations. More details of the variations are discussed in Sections 4.3 and 4.4.

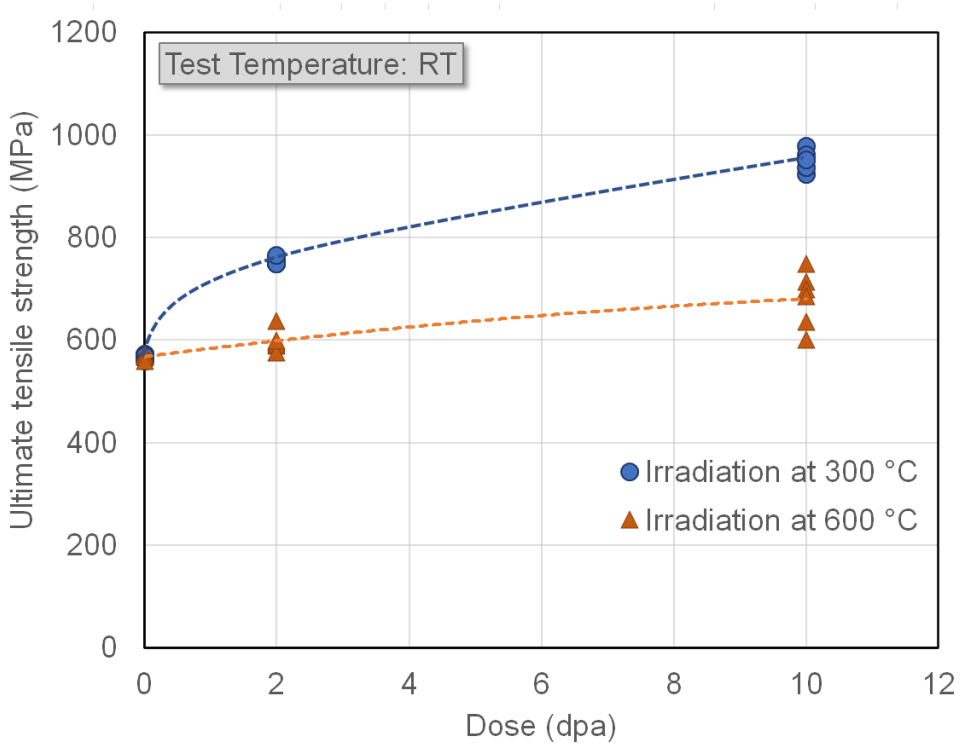

Figure 7. Effect of neutron irradiation on ultimate tensile strength at room temperature

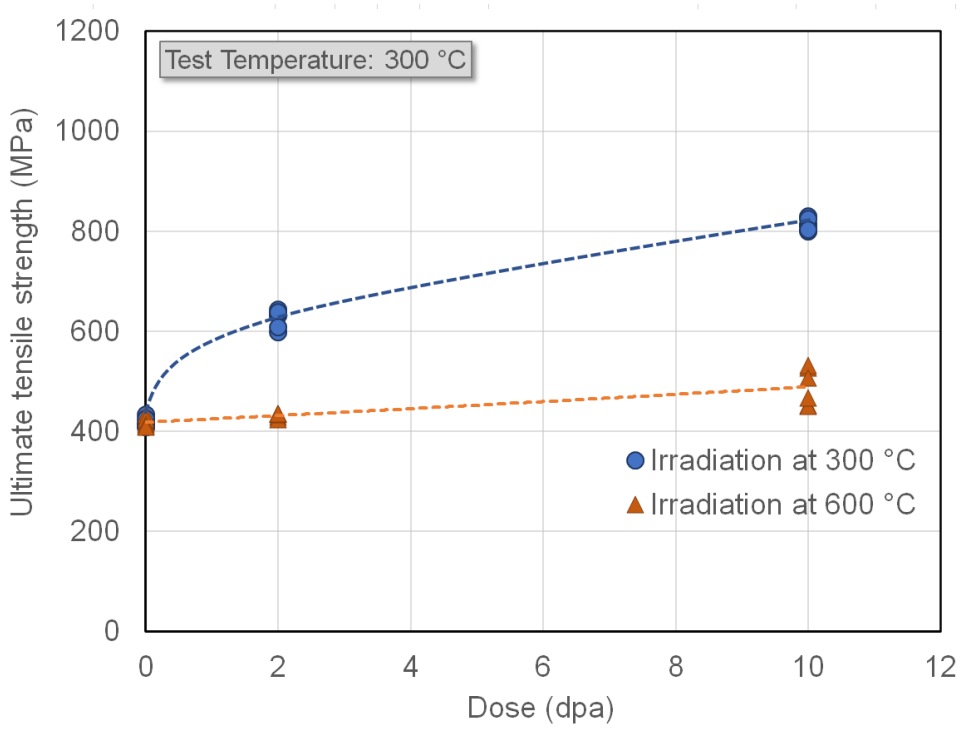

Figure 8. Effect of neutron irradiation on ultimate tensile strength at 300 °C

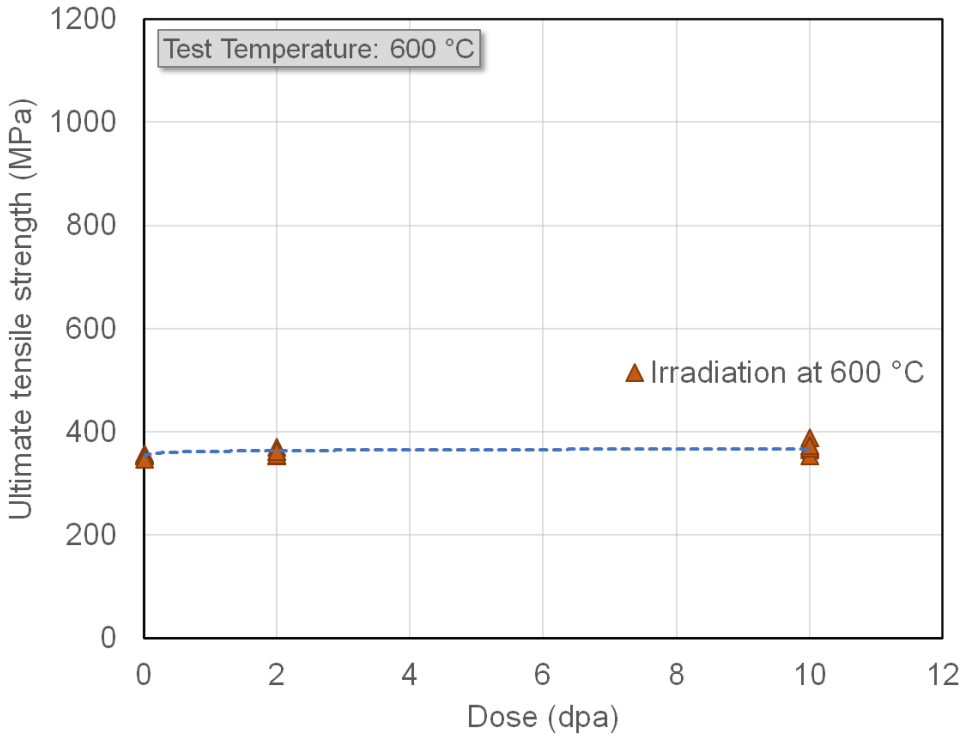

Figure 9. Effect of neutron irradiation on ultimate tensile strength at 600 °C

4.2 Dependence of Ductility on Irradiation Dose and Temperature

The effects of irradiation on uniform and total ductility (UE and TE) are summarized in Figures 10 through 15. Among the engineering tensile parameters, UE is the parameter that can be most sensitive to the irradiation condition and the percent increase or decrease caused by the irradiation effect is often the largest. When the irradiation temperature is relatively low or in the 300 °C irradiation of this campaign, the loss of uniform ductility is swift and substantial as displayed in Figures 10 and 11. In the room temperature testing, the uniform elongation decreased from ~55% before irradiation to ~15% at 2 dpa and to ~1% at 10 dpa. The loss of uniform ductility at 300 °C is more substantial: UE decreased from ~20% to ~3 % at 2 dpa and to < 0.5 % at 10 dpa. Considering the gradually spreading nature of plasticity in small scale, it is concluded that the AM 316 steels after low temperature (300 °C) irradiation completely lose uniform ductility at 300 °C.

Meanwhile, the reduction of total elongation after 600°C irradiation is moderate, as shown in Figures 10 through 12. At room temperature, the irradiated 316L materials show slow decrease in TE with dose, but significant variation is observed each six-component dataset. In the testing at 300°C, the UE data after irradiation demonstrate a small increase at 2 dpa and a small decrease at 10 dpa. This ductility increase–decrease cycle is more obvious in the 600°C testing, as shown in Figure 12. The increase of ductility during irradiation is called the radiation-induced ductilization [34,35], and the AM 316 materials have demonstrated weak radiation-induced ductilization in the earlier campaign **[**26**]**. Although the ductilization by irradiation is a beneficial phenomenon that can mitigate a material's radiation-induced property degradation, the current results indicate that it is a temporary phenomenon that appears only in a small dose range.

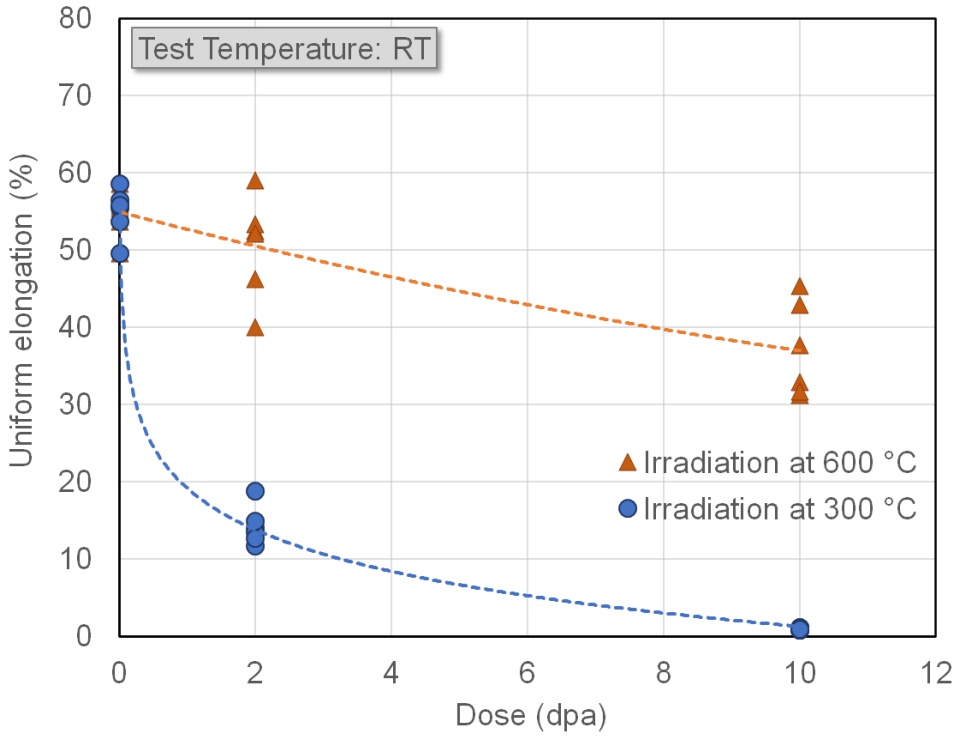

Figure 10. Effect of neutron irradiation on uniform elongation at room temperature

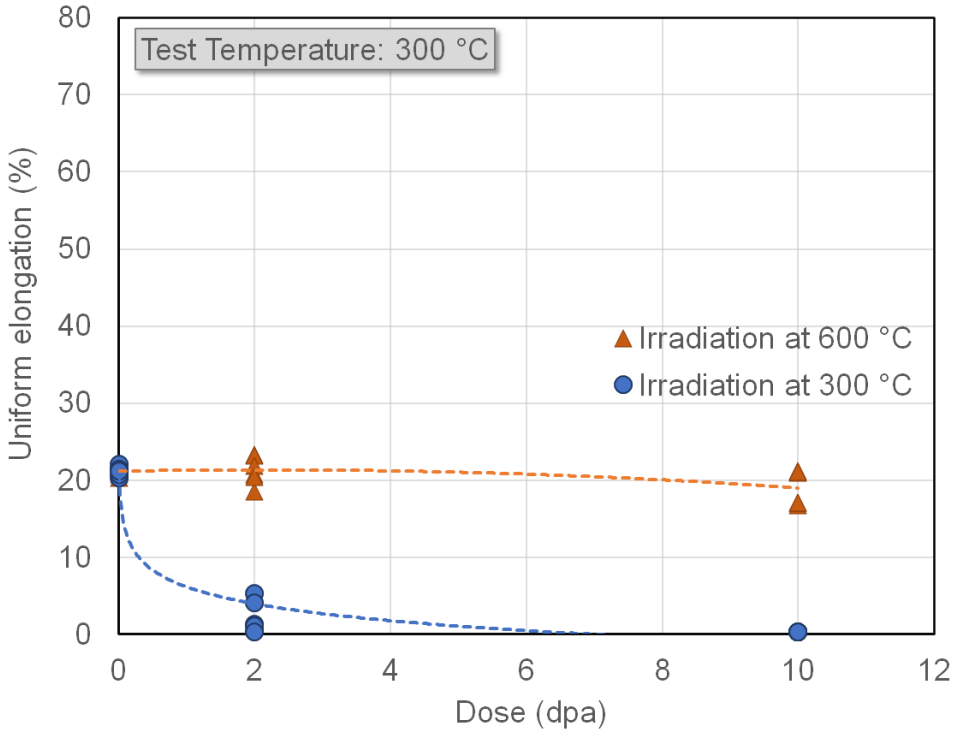

Figure 11. Effect of neutron irradiation on uniform elongation at 300 °C

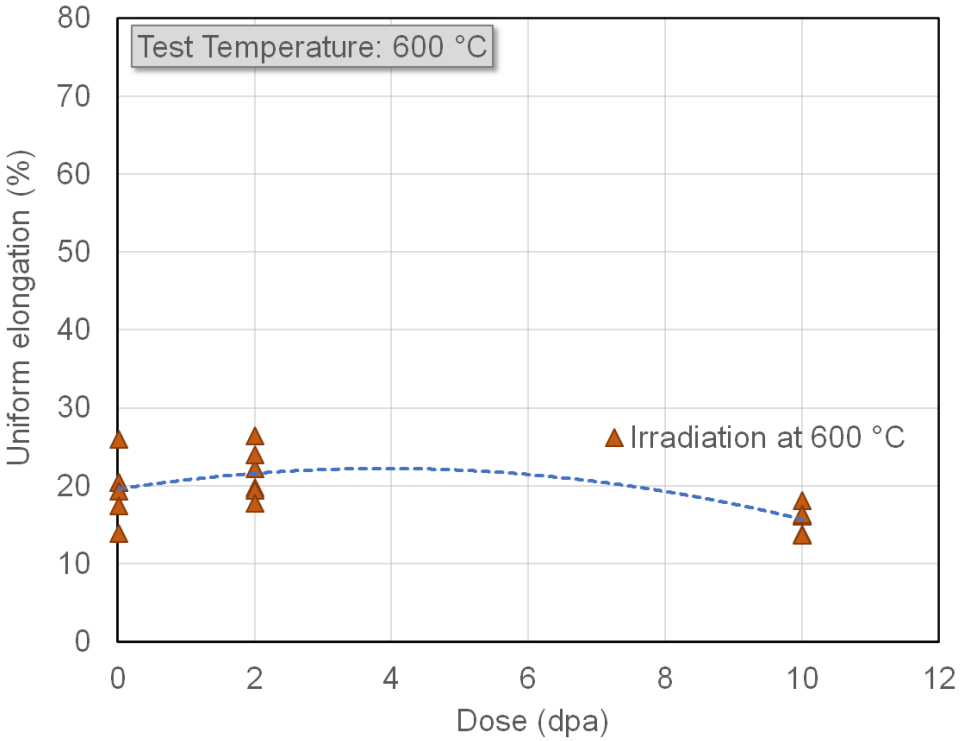

Figure 12. Effect of neutron irradiation on uniform elongation at 600 °C

As displayed in Figures 13 through 15, the overall post-irradiation behavior measured by TE, including its dependence on test and irradiation conditions, is very similar to that of UE as the UE value is a major portion of a TE value and the necking ductility (TE-UE) tends to be less dependent on irradiation conditions if ductile deformation dominates. Regardless of the low UE cases after 300 °C irradiation, all the tensile test results in the research have shown ductile deformation and failure, and the necking ductility is at least more than a few percent engineering strain and is relatively consistent throughout the test and irradiation conditions. Furthermore, all the engineering strains measured for the necking ductility are within a range of 5 to 20%. Therefore, the discussion on UE data should be the same for the TE data, except for a few minor deviations, such as the ratios between the measured parameters.

The data variation within each six-component dataset is at the largest level in the few TE datasets after 600 °C irradiation. The degree of data scattering is particularly large in the datasets obtained at room temperature after 600 °C irradiation, as shown in Figure 13. Further comparison and discussion on this observation will be given in the next section. Moreover, the ductilization phenomenon measured by TE is minimal: Figure 15 shows a very small or subtle increase in TE at 2 dpa.

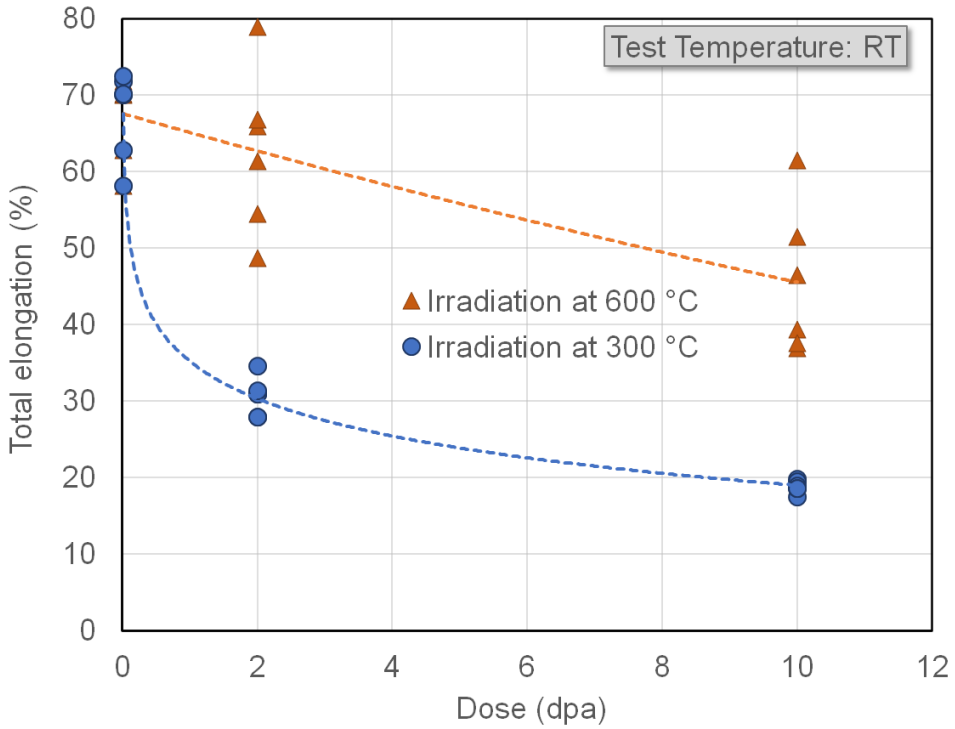

Figure 13. Effect of neutron irradiation on total elongation at room temperature

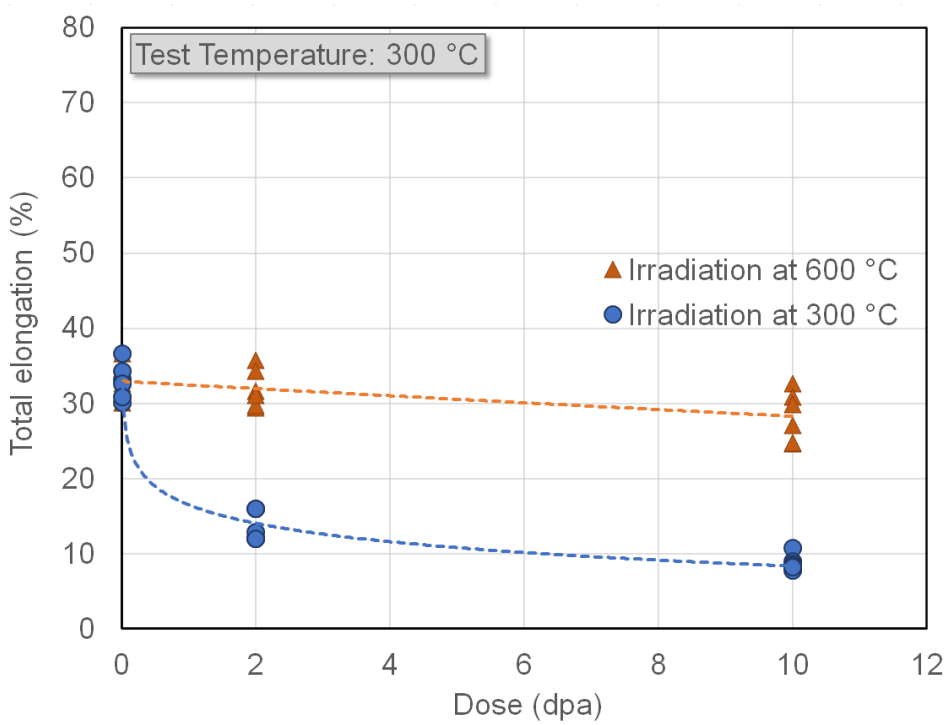

Figure 14. Effect of neutron irradiation on total elongation at 300 °C

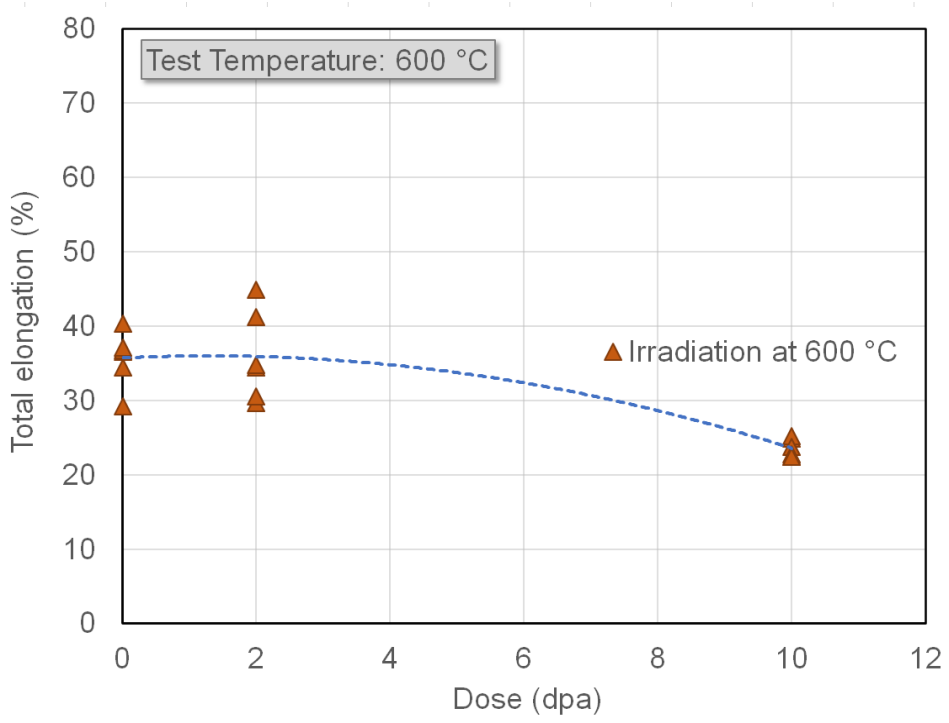

Figure 15. Effect of neutron irradiation on total elongation at 600 °C

4.3 Strength and Ductility in Different Materials Conditions

This section provides tensile property data for 316L SS—strength (YS) and ductility (TE) data before and after irradiation in various microstructure conditions—primarily for comparison. That is, the tensile test data before and after irradiation were the main contents in the milestone report of FY 2021 [26], and the YS and TE data displayed in Figures 16 and 17 are given in this section as reference data. As briefly mentioned previously, the uniaxial tensile property data of 316L alloy were obtained before and after irradiation using SS-J2 specimens with four different microstructural conditions: additively manufactured AM 316L alloy in the as-built, stress-relieved (650°C/1 h), and solution-annealed (1,050°C/1 h) conditions and reference 316L alloy in wrought (WT: hot-rolled and solution-annealed) condition [11,26]. To elucidate the effects of microstructural variation on the postirradiation performance, tensile testing was performed at room temperature, 300°C (and 260°C and 390°C), 500°C, and 600°C for the specimens irradiated to 0.2 and 2 dpa at target temperatures of 300°C and 600°C.

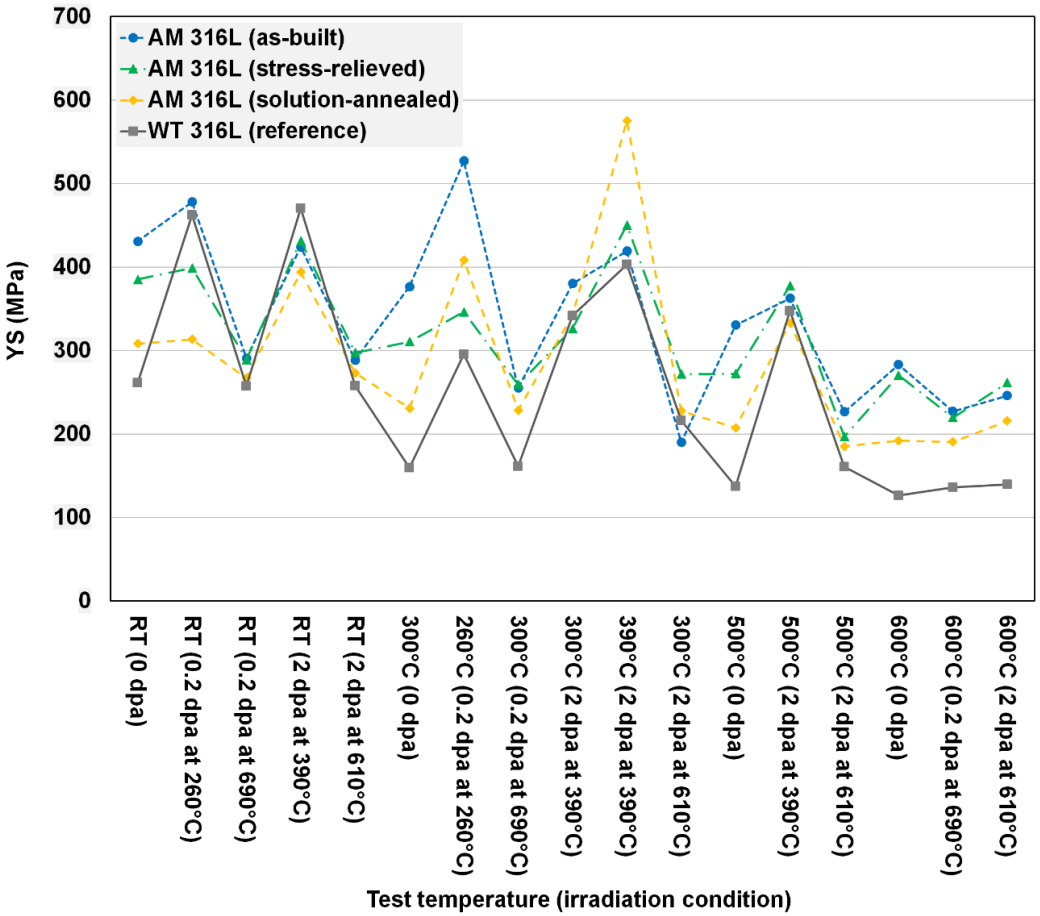

Figure 16. YS data for AM and WT 316L SSs in various irradiation conditions

Comparing the irradiation and PIE matrices for this campaign (CTGR-7 to CTGR-10) and earlier campaign (CTGR-1 to CTGR-6), multiple cases included tensile specimens that were postbuild treated and irradiated in the same target conditions: the tensile property data for the stress-relieved AM 316L alloy irradiated to 0.2 or 2 dpa at 300°C and 600°C and tested at room temperature, 300°C, and 600°C. Some YS and TE data in green color in Figures 16 and 17 are directly comparable to the data discussed in the previous sections. A comparison of YS data in Figures 4 through 6 with the those in Figure 16 in the

corresponding conditions confirms that the data from both campaigns are mostly within the ordinary scattering range of experimental data. An exception is found for the case with a target temperature of 300°C: the YS data at 2 dpa from the two campaigns showed evident differences because the actual irradiation temperature in the first campaign was much higher (i.e., 396°C) than the target temperature. Comparison of TE data also yielded a similar result: matching TE data in Figure 18 are within the data scattering span in each data cluster in Figures 13 through 15, except for one irradiation case (2 dpa, 396°C) that showed higher TE out of the large TE data scattering range observed in this campaign.

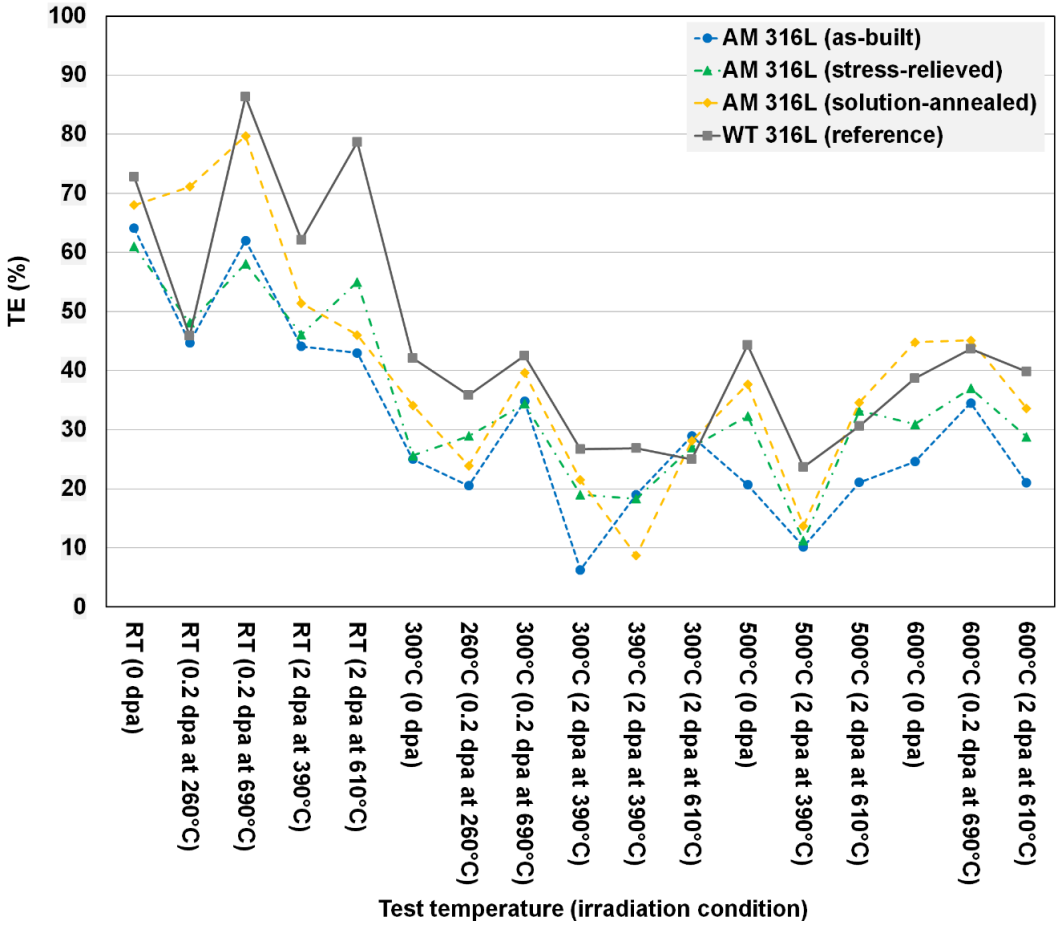

Figure 17. TE data for AM and WT 316L SSs in various irradiation conditions

4.4 Location Dependence of Strength after Irradiation

The sampling location dependencies of engineering tensile properties are elucidated in this section for strength parameters (YS and UTS) and in the next section for ductility parameters (UE and TE). Discussion and analysis aimed to find any consistent phenomena that would be considered as the effects of different sampling locations on the postirradiation property changes in the AM 316L steels. The sampling location dependence was relatively small in strength parameters, and many six-component datasets, representing respective sampling locations, showed small variations among their values. These variations are considered well within the ordinary experimental error range. Therefore, this and following

sections discuss selected datasets that exhibit significant variations, which are coupled with the tensile property vs. dose plots used in the earlier sections.

Figure 18 is the room temperature UTS vs. dose plot associated with the two graphs, each of which displays individual UST data that belong to the dataset. The UTS datasets after higher temperature (600°C) irradiation show relatively larger variations compared with those after lower temperature (300°C) irradiation. This trend is consistently observed in the other parameters in the following discussion. In the room temperature UTS dataset after 2 dpa/600°C irradiation, a maximum UTS was observed from the specimen sampled from the 40 mm cube surface, whereas at 10 dpa the maximum UTS was from the center layer of the cube. In the YS and UTS datasets from 300°C testing (Figure 19), the maximum YS after 2 dpa/300°C irradiation was obtained from the cube surface layer. However, the graph for the UTS dataset after 10 dpa/600°C irradiation shows that a maximum value was obtained from the center layer of the 5 mm plate. These checks in the strength data behavior do not indicate any consistent pattern in the effect of sampling location on irradiation response of the test materials. Some possible influencing factors, such as the surface vs. interior layers and the thickness of the build, which may affect the cooling rate, may be considered as the cause of the strength variations; however, direct comparisons among the strength datasets lead to the same conclusion.

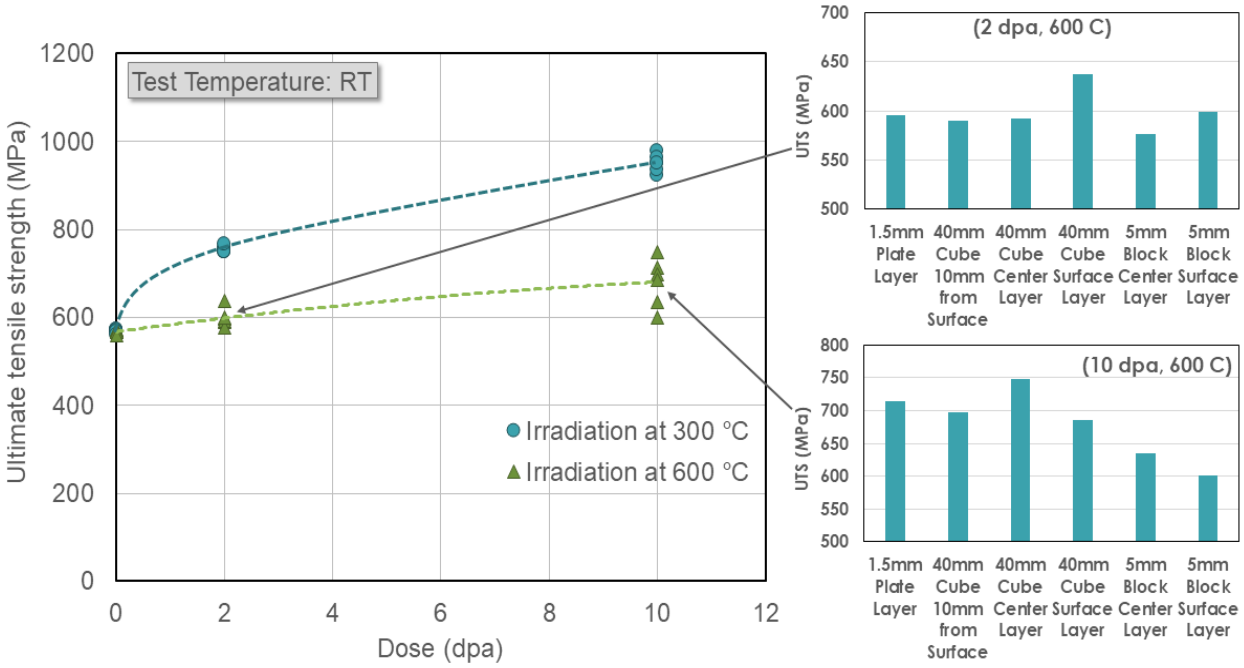

Figure 18. Sampling location dependence in UTS data measured at room temperature after 600 °C irradiation

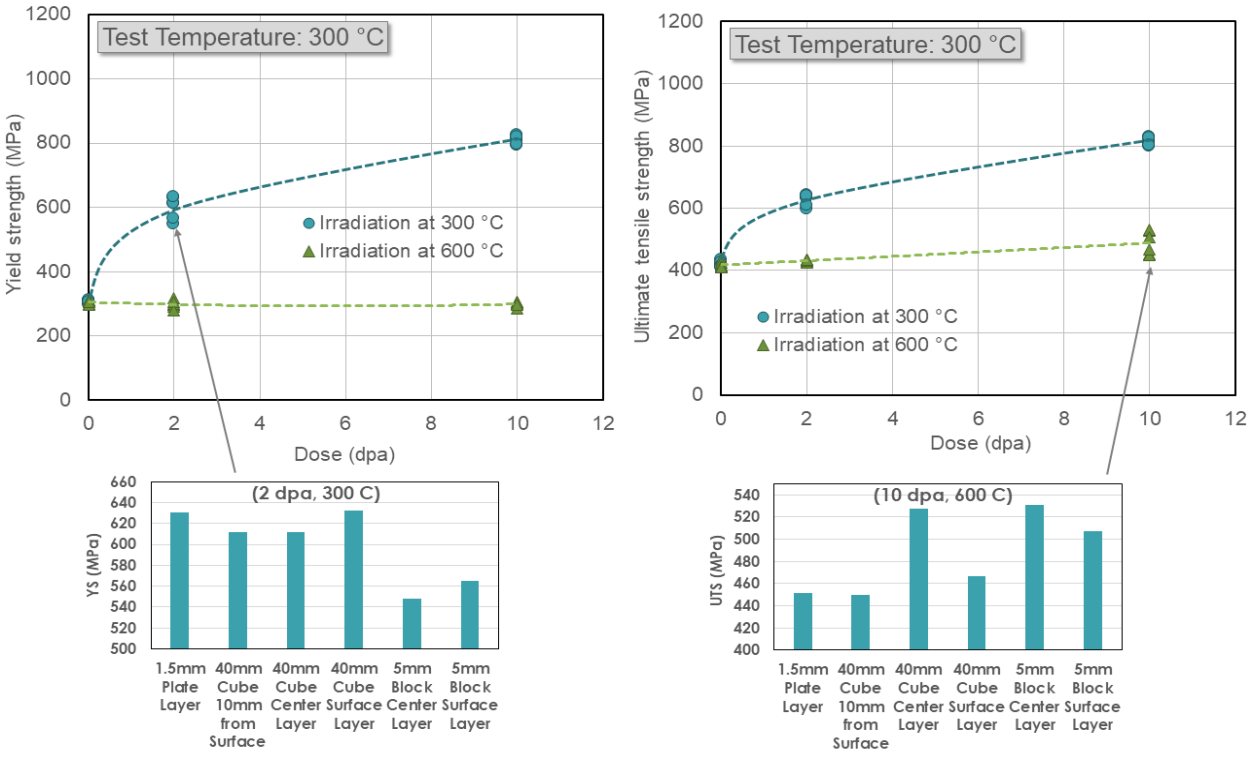

Figure 19. Sampling location dependence in YS and UTS data measured at 300 °C after irradiation

4.5 Location Dependence of Ductility after Irradiation

Ductility parameters are generally more sensitive to the microstructure because the UE and TE data are measured, respectively, after consuming all uniform deformation capability and at the final failure. Therefore, the initial microstructure can evolve and affect the deformation and failure modes in both microscopic and macroscopic scales. This general behavior of materials seems to be well reflected in the ductility datasets after irradiation: overall, much larger variations were observed in the ductility datasets displayed in Figures 20 24 compared with those discussed in the previous section.

Figures 20 and 21 compare the UE datasets in different test and irradiation conditions, respectively, from the room temperature and 600°C tests. Figure 20 shows that the variations in UE data after 600°C irradiation are significantly larger than those after lower temperature irradiation. Maximum UE values were measured from the specimens from the 1.5 mm plate layer and the 5 mm block center layer, and the maximum data span in the dataset of 2 dpa/600°C irradiation case was about 20%. In Figure 21, which displays 600°C irradiation data only, the 1.5 mm plate layer and intermediate layer (10 mm from surface) of 40 mm cube showed maximum UE values. As with the strength data, this observation on UE data behavior leads to the same conclusion that no consistent relationship between the sampling location and the tensile properties before and after irradiation is found, at least, with the current sets of tensile data. The variation in UE data from room temperature testing increases with irradiation dose, whereas those from 600°C testing decrease with irradiation dose. This trend is believed to be a random behavior because no consistent behavior are observed with other parameters. Finally, a notable observation in the comparison between the tensile datasets with different testing temperatures is that the room temperature datasets show generally higher variation than those at elevated temperatures. This behavior might be important: it is commonly observed in different parameters.

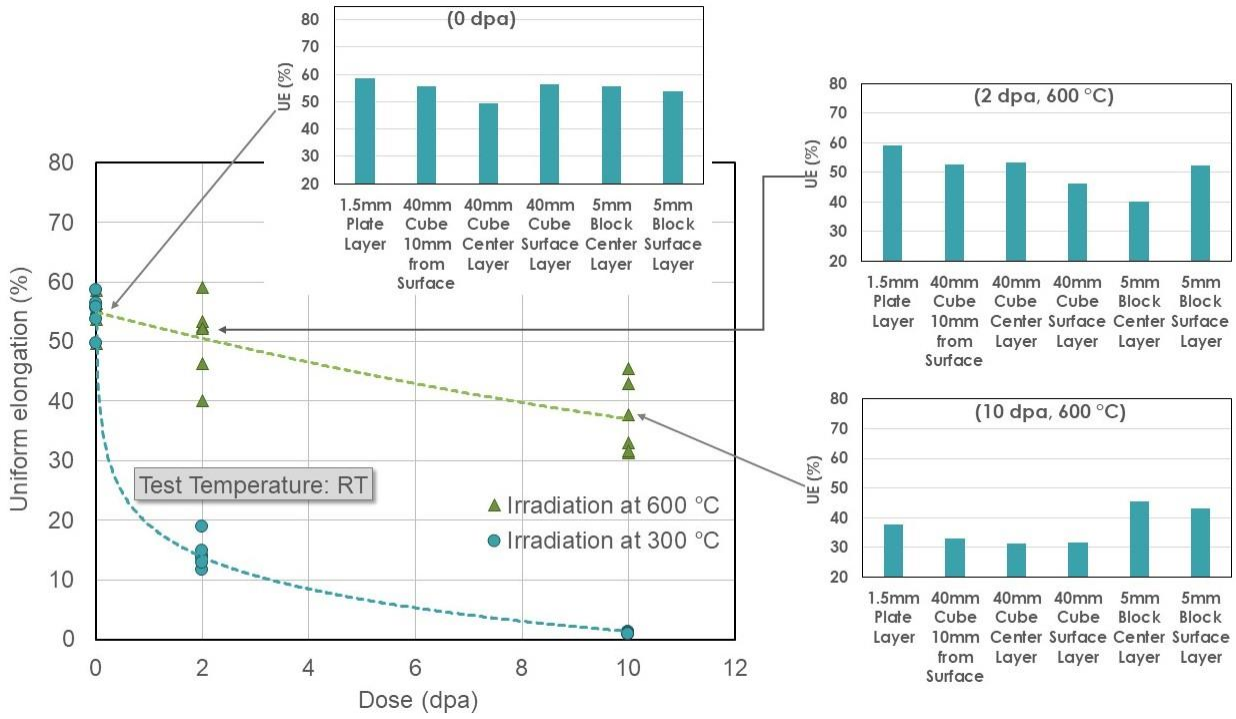

Figure 20. Sampling location dependence in UE data measured at room temperature before and after irradiation

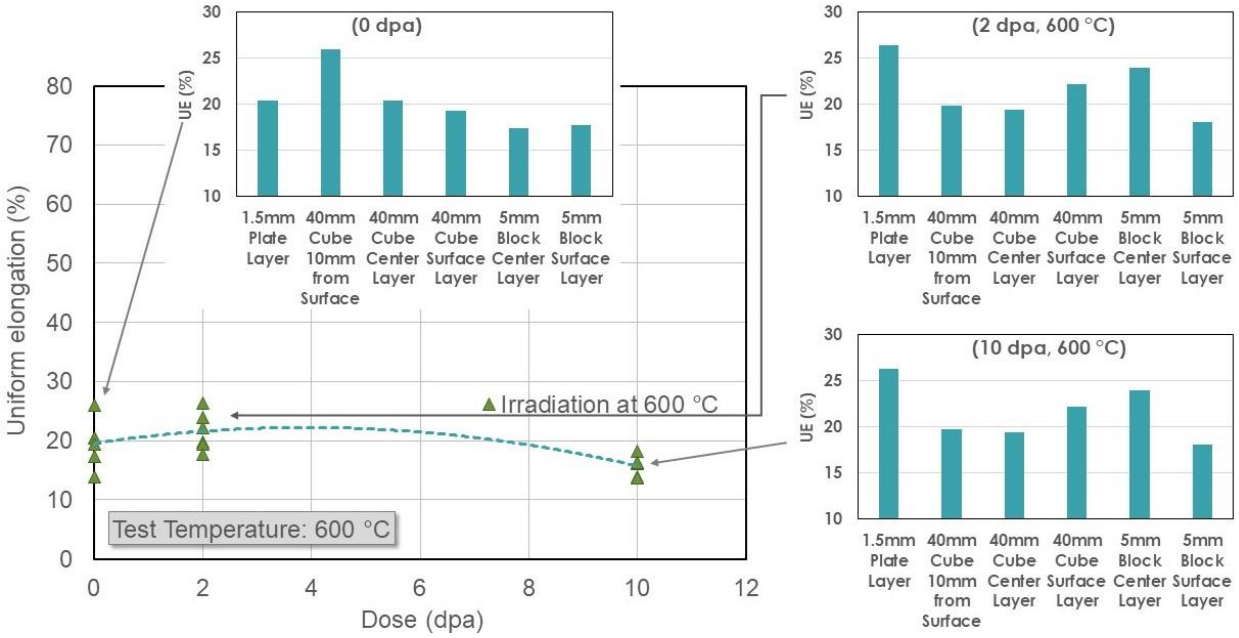

Figure 21. Sampling location dependence in UE data measured at 600 °C before and after 600 °C irradiation

The variation in TE datasets is generally largest among the tensile property parameters. The largest difference of ~32 % strain is observed in the dataset from room temperature testing after 2 dpa/600 °C

irradiation (Figure 22), where the largest variation of UE data is also observed (see Figure 20). As shown in Figures 23 and 24, the variation within a dataset becomes smaller at higher test temperatures. It is particularly small in the 600 °C tested specimens after 10 dpa/600 °C irradiation, for which an obvious ductility reduction is observed after the increased ductility at 2 dpa. Furthermore, as shown in Figure 20, the neutron irradiation at 300 °C resulted in smaller data scattering than other irradiation conditions.

Regarding the sampling location dependence of the AM 316L steels, no consistent behavior is observed in the TE datasets. Throughout the TE datasets displayed in this report, the maximum TE value is observed in the specimens machined from either the 1.5 mm plate or the center layer of the 5 mm plate. It can be tentatively concluded that the thinner plates can result in higher ductility, but this conclusion cannot be applied to all datasets in the study. Furthermore, all ductility datasets taken before irradiation show significant variations, as shown in the displayed data in Figures 20 through 24.

The austenitic SSs usually develop very fine grain microstructures with well-developed dislocation cell structures during the AM process [36-39] and experience a slight relaxation in dislocation structure by stress-relieving treatment [11,26]. The initial microstructure exposed to irradiation, or the AM-built and stress-relieved microstructure, is actually a slightly metastable structure [26]. Consequently, any activation by irradiation will induce significant microstructural reactions in addition to the defects generated by irradiation. Therefore, the alloy microstructure in as-built and post-AM treated condition will evolve into a new structure during irradiation, gradually affecting the mechanical properties with increasing irradiation dose. However, the evolution in the AM 316L microstructure (in stress relieved condition) during neutron irradiation is poorly understood and requires comprehensive future work.

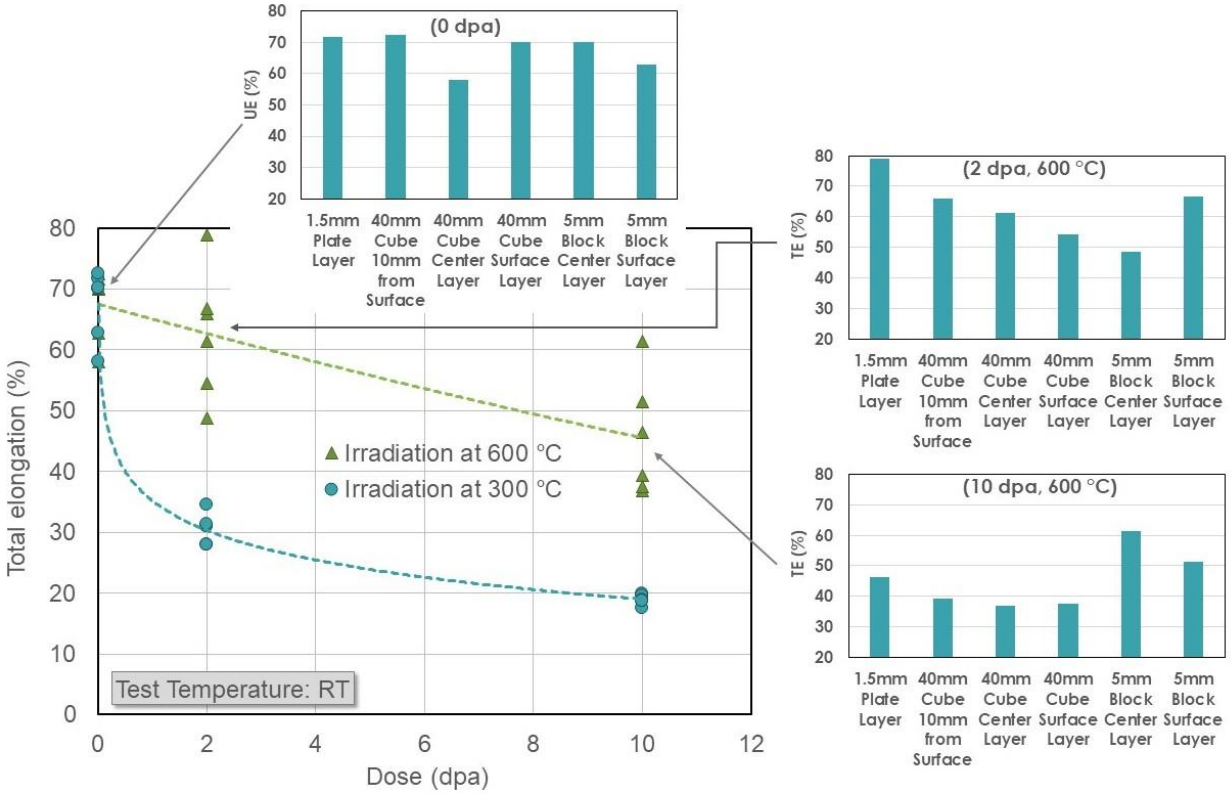

Figure 22. Sampling location dependence in TE data measured at room temperature before and after irradiation

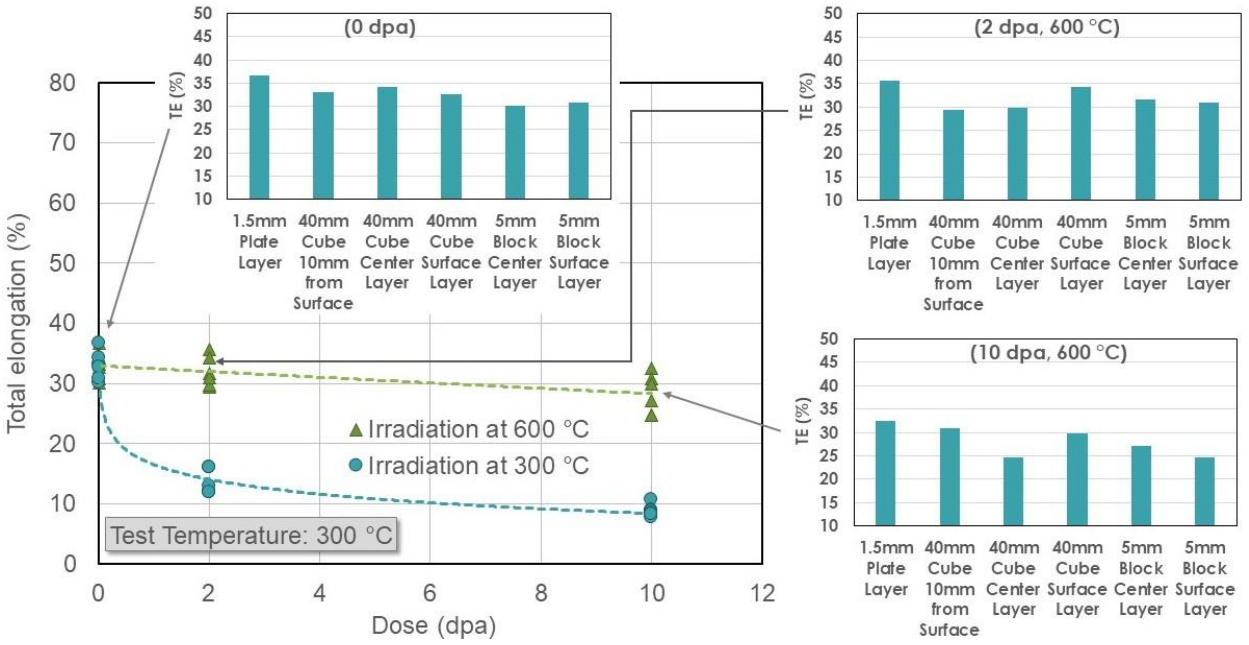

Figure 23. Sampling location dependence in TE data measured at 300 °C before and after irradiation

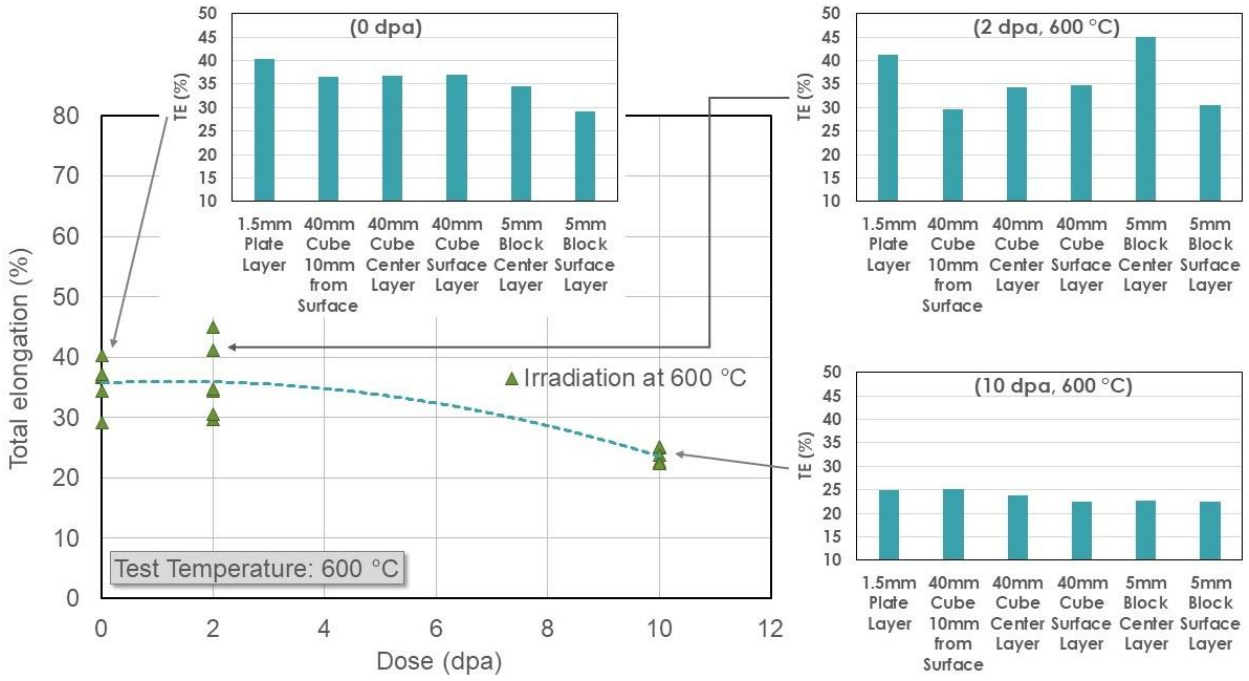

Figure 24. Sampling location dependence in TE data measured at 600 °C before and after 600 °C irradiation

5. CONCLUDING REMARKS

[1]. Mechanical and physical property data for the AM 316L steels before and after neutron irradiation have been accumulated for the AMMT program to build a materials property handbook and assess the AM materials for nuclear reactor applications. The testing and evaluation task in the FY2023 Campaign-2 elucidated the effects of sampling location and build size on the mechanical properties before and after irradiation. The SS-J3 tensile specimens were irradiated in HFIR to 2 and 10 dpa at the target temperatures of 300 °C and 600 °C, and the post-irradiation tensile testing was performed at room temperature, 300 °C, and 600 °C, which was the second large PIE campaign for the program.

[2]. The mechanical properties of AM 316L steel were significantly influenced by the characteristic microstructures of printed materials, which include fine grains and high-density dislocations and result in higher initial strength and lower ductility compared with the traditional 316L steel. Regardless of sampling location, the AM 316L steel retained relatively high strength and ductility to the highest irradiation dose of 10 dpa compared with the traditional 316L steel. A prompt necking at yield (showing little uniform ductility) was observed after irradiation at 300 °C but no embrittlement was observed up to 10 dpa. Ductilization by irradiation–the radiation-induced increase of ductility–was observed for the 600 °C irradiation and it occurred in low dose range (0.2 and 2 dpa) only.

[3]. Although inhomogeneous mechanical properties owing to different sampling locations were expected to be significant, no consistent dependencies of strength and ductility on sampling location were observed for different build thicknesses and sampling locations. The ductility data (UE and TE) tend to show larger variation within each six-component dataset compared with the strength data (YS and UTS).

[4]. The neutron irradiation has significantly increased the variation in tensile property data, particularly after 600 °C irradiation, although no clear dependence of tensile properties on build thickness or sampling location was confirmed. Furthermore, regardless of irradiation condition, the variation within a dataset was minimum in the 300 °C test data.

6. REFERENCES

[1] S. J. Zinkle, J. T. Busby, "Structural materials for fission & fusion energy," *Materials Today*, 12 (2009) 12-19.

[2] P. J. Maziasz and J. T. Busby, "Properties of Austenitic Steels for Nuclear Reactor Applications," *Comprehensive Nuclear Materials*, 2 (2012) 267–283.

[3] "Structural Materials for Liquid Metal Cooled Fast Reactor Fuel Assemblies-Operational Behavior," *IAEA Nuclear Energy Series, NF-T-4.2*, 2012.

[4] S. Sahin, M. Übeyli, "A Review on the Potential Use of Austenitic Stainless Steels in Nuclear Fusion Reactors," *J. Fusion Energy*, 27 (2008) 271–277.

[5] A. A. Tavassoli, "Assessment of Austenitic Stainless Steels," *Fusion Engineering and Design*, 29 (1995) 371–390.

[6] V. Karthik, S. Murugan, P. Parameswaran, C. N. Venkiteswaran, K. A. Gopal, N. G. Muralidharan, S. Saroja, K. V. Kasiviswanathan, "Austenitic Stainless Steels for Fast Reactors -Irradiation

Experiments, Property Evaluation and Microstructural Studies," *Energy Procedia*, 7 (2011) 257–263.

[7] "Austenitic Stainless Steels," in *Stainless Steels for Design Engineers*, ASM International, 2008.

[8] K.G. Field, J. Simpson, M. N. Gussev, H. Wang, M. Li, X. Zhang, X. Chen, T. Koyanagi, K. Kane, A. Marquez Rossy, M. Balooch, and K.A. Terrani, "Handbook of Advanced Manufactured Material Properties from TCR Structure Builds at ORNL – FY19," ORNL/TM-2019/1328, Oak Ridge National Laboratory, 2019.

[9] J. Simpson, J. Haley, C. Cramer, O. Shafer, A. Eilliott, W. Peter, L. Love, R. Dehoff, "Considerations for Application of Aadditive Manufacturing to Nuclear Reactor Core Components," ORNL/TM-2019-1190, Oak Ridge National Laboratory, 2019.

[10] T. S. Byun, M. N. Gussev, T. G. Lach, M. R. McAlister, J. J. Simpson, B. E. Garrison, Y. Yamamoto, C. B. Joslin, J. K. Carver, F. A. List, R. R. Dehoff, K. A. Terrani, M. Li, X. Zhang, "Mechanical Properties and Deformation Behavior of Additively Manufactured 316L Stainless Steel – FY 2020," ORNL/TM-2020/1574, Oak Ridge National Laboratory, 2020.

[11] T.S. Byun, B.E. Garrison, M.R. McAlister, X. Chen, M.N. Gussev, T.G. Lach, A. Le Coq, K. Linton, et al., "Mechanical behavior of additively manufactured and wrought 316L stainless steels before and after neutron irradiation," *J. Nucl. Mater.*, 548 (2021) 152849.

[12] B. M. Morrow, T. J. Lienert, C. M. Knapp, J. O. Sutton, M. J. Brand, R. M. Pacheco, V. Livescu, J. S. Carpenter, G. T. Gray, "Impact of Defects in Powder Feedstock Materials on Microstructure of 304L and 316L Stainless Steel Produced by Additive Manufacturing," *Metall. Mater. Trans. A*, 49 (2018) 3637–3650.

[13] T. Ronneberg, C. M. Davies, and P. A. Hooper, "Revealing Relationships between Porosity, Microstructure and Mechanical Properties of Laser Powder Bed Fusion 316L Stainless Steel through Heat Treatment," *Mater. Des.*, 189 (2020) 108481.

[14] A. J. Birnbaum, J. C. Steuben, E. J. Barrick, A. P. Iliopoulos, J. G. Michopoulos, "Intrinsic Strain Aging, Σ3 Boundaries, and Origins of Cellular Substructure in Additively Manufactured 316L," *Addit. Manuf.*, 29 (2019) 100784.

[15] U. S. Bertoli, B .E. MacDonald, J. M. Schoenung, "Stability of Cellular Microstructure in Laser Powder Bed Fusion of 316L Stainless Steel," *Mater. Sci. Eng. A*, 739 (2019) 109–117.

[16] M. Li, X. Zhang, W.Y. Chen, F. Heidet, "Progress Report on the Assessment of the Material Performance for TCR Applications," ANL/NSE-20/12, Argonne National Laboratory, 2020.

[17] T. Kurzynowski, K. Gruber, W. Stopyra, B. Kuźnicka, E. Chlebus, "Correlation between Process Parameters, Microstructure and Properties of 316 L Stainless Steel Processed by Selective Laser Melting," *Mater. Sci. Eng. A*, 718 (2018) 64–73.

[18] C. R. Brinkman, "Elevated-Temperature Mechanical Properties of an Advanced Type 316 Stainless Steel, United States," ORNL/CP-101053, Oak Ridge National Laboratory, 1999.

[19] E. Garlea, H. Choo, C. C. Sluss, M. R. Koehler, R. L. Bridges, X. Xiao, Y. Ren, B. H. Jared, "Variation of Elastic Mechanical Properties with Texture, Porosity, and Defect Characteristics in Laser Powder Bed Fusion 316L Stainless Steel," *Mater. Sci. Eng. A*, 763 (2019) 138032.

[20] T. Pinomaa, M. Lindroos, M. Walbrühl, N. Provatas, A. Laukkanen, "The Significance of Spatial Length Scales and Solute Segregation in Strengthening Rapid Solidification Microstructures of 316L Stainless Steel," *Acta Mater.*, 184 (2020) 1–16.

[21] M. Li, X. Zhang, W.Y. Chen, F. Heidet, T. S. Byun, K.A. Terrani, "Creep Behavior of 316L Stainless Steel Manufactured by Laser Powder Bed Fusion," *J. Nucl. Mater.,* 548 (2021) 152847.

[22] D. Kong, X. Ni, C. Dong, L. Zhang, C. Man, X. Cheng, and X. Li, "Anisotropy in the Microstructure and Mechanical Property for the Bulk and Porous 316L Stainless Steel Fabricated via Selective Laser Melting," *Mater. Lett. ,* 235 (2019) 1–5.

[23] J. Lin, F. Chen, X. Tang, J. Liu, S. Shen, and G. Ge, "Radiation-Induced Swelling and Hardening of 316L Stainless Steel Fabricated by Selected Laser Melting," *Vacuum,* 174 (2020) 109183.

[24] M. Song, M. Wang, X. Lou, R. B. Rebak, and G. S. Was, "Radiation Damage and Irradiation-Assisted Stress Corrosion Cracking of Additively Manufactured 316L Stainless Steels," *J. Nucl. Mater.,* 513 (2019) 33–44.

[25] G. Meric de Bellefon, K.M. Bertsch, M.R. Chancey, Y.Q. Wang, D.J. Thoma, "Influence of solidification structures on radiation-induced swelling in an additively-manufactured austenitic stainless steel," *J. Nucl. Mater.,* 523 (2019) 291-298.

[26] TS Byun, David Collins, Annabelle Le Coq, Tim Lach, Kory Linton, Maxim N Gussev, Jesse Werden, Michael Mcalister, Xiang Chen, Chase Joslin, Keith Carver, Fred List III, "Mechanical Properties of Additive Manufacturing 316L Stainless Steel Before and After Neutron Irradiation-FY 2021," Oak Ridge National Laboratory, ORNL/TM-2021/2121 (M2TC-21OR0403032).

[27] A. G. Le Coq, K. D. Linton, P. Champlin, R. H. Howard, X. Hu, T. S. Byun, K. A. Terrani, "HFIR Irradiation Testing Supporting the Transformational Challenge Reactor," ANS Trans. (2020) 242–245.

[28] P. Champlin, J. Burns, C. Petrie, X. Hu, K. D. Linton, R. Howard, K. A. Terrani, "Capsule and Specimen Geometries for HFIR Irradiation Testing Supporting the Transformational Challenge Reactor," ORNL/TM-2019/1310, Oak Ridge National Laboratory, 2019.

[29] S. Taller, A. Le Coq, C. Massey, J. Werden, M. Lynch, K. Linton, "Report on Evolution of Inconel 718 Following HFIR Irradiation," ORNL/TM-2022/2600, Oak Ridge National Laboratory, Oak Ridge, TN, September 2022.

[30] K. Farrell, T. S. Byun, "Tensile properties of candidate SNS target container materials after proton and neutron irradiation in the LANSCE accelerator," *J. of Nucl. Mater.,* 296 (1-3) (2001) 129–138.

[31] ASTM E8 / E8M, Standard Test Methods for Tension Testing of Metallic Materials, ASTM International, 2016.

[32] ASTM E21, Standard Test Methods for Elevated Temperature Tension Tests of Metallic Materials, ASTM International, 2020.

[33] D.J. Edwards, E.P. Simonen, S.M. Bruemmer, "Evolution of fine-scale defects in stainless steels neutron-irradiated at 275 C," *J. Nucl. Mater.,* 317 (2003) 13–31.

[34] Y. Kitsunai, H. Kurishita, T. Kuwabara, M. Narui, M. Hasegawa, T. Takida, K. Takebe, "Radiation embrittlement behavior of fine-grained molybdenum alloy with 0.2 wt¾TiC addition," *J. Nucl. Mater.,* 346 (2005) 233- 243.

[35] A. Hishinuma, K. Fukai, T. Sawai, K. Nakata, "Ductilization of TiAl intermetallic alloys by neutron-irradiation," *Intermetallics,* pp. 4 (1996) 179-184.

[36] Y.M. Wang, T. Voisin, J.T. McKeown, J. Ye, N. P. Calta, Z. Li, Z. Zeng, Y. Zhang, W. Chen, T. T. Roehling, R. T. Ott, M. K. Santala, P. J. Depond, M. J. Matthews, A. V. Hamza, T. Zhu,

"Additively Manufactured Hierarchical Stainless Steels with High Strength and Ductility," *Nat. Mater.*, 17 (2018) 63–71.

[37] S. Li, J. Hu, W.-Y. Chen, J. Yu, M. Li, and Y. Wang, "Evolution of Cellular Dislocation Structures and Defects in Additively Manufactured Austenitic Stainless Steel under Ion Irradiation," *Scr. Mater.* , 178 (2020) 245–250.

[38] Y. Zhong, L. Liu, S. Wikman, D. Cui, and Z. Shen, "Intragranular Cellular Segregation Network Structure Strengthening 316L Stainless Steel Prepared by Selective Laser Melting," *J. Nucl. Mater.*, 470 (2016) 170–178.

[39] Shilei Li, Jing Hu, Wei-Ying Chen, Jingyue Yu, Meimei Li, Yandong Wang,, "Evolution of cellular dislocation structures and defects in additively manufactured austenitic stainless steel under ion irradiation," *Scripta Mater.*, 178 (2020) 245-250.

7. APPENDIX

This Appendix displays the engineering stress-strain curves generated from raw-data files using measured dimension data. In each graph, six tensile curves for the six sampling locations are plotted together. Table A1 lists all 13 figure numbers, along with their irradiation and test conditions.

Table A1. List of engineering stress-strain curves

Figure No.	Target Irradiation Temp. (°C)	Dose (dpa)	Test Temp. (°C)	Capsule ID
Fig. A1	–	0	25	Control
Fig. A2	–	0	300	Control
Fig. A3	–	0	600	Control
Fig. A4	300	2	25	GTCR07
Fig. A5	600	2	25	GTCR08
Fig. A6	300	10	25	GTCR09
Fig. A7	600	10	25	GTCR10
Fig. A8	300	2	300	GTCR07
Fig. A9	600	2	300	GTCR08
Fig. A10	300	10	300	GTCR09
Fig. A11	600	10	300	GTCR10
Fig. A12	600	2	600	GTCR08
Fig. A13	600	10	600	GTCR10

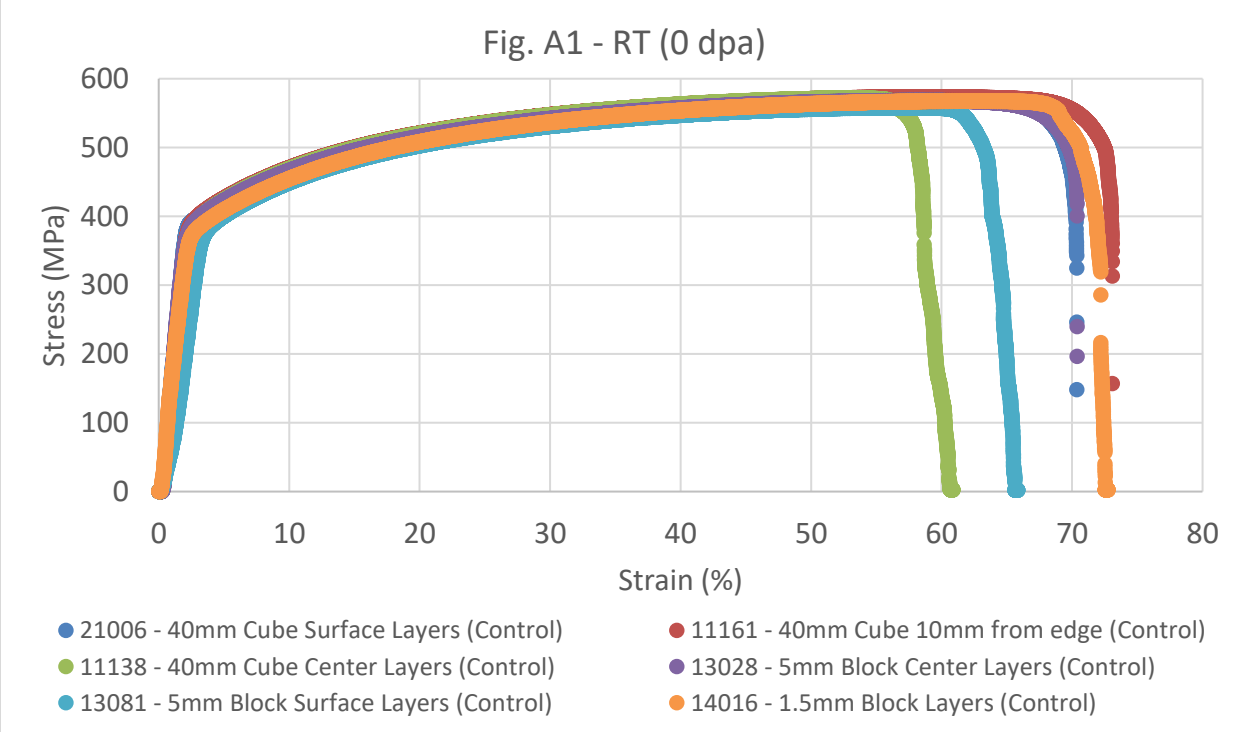

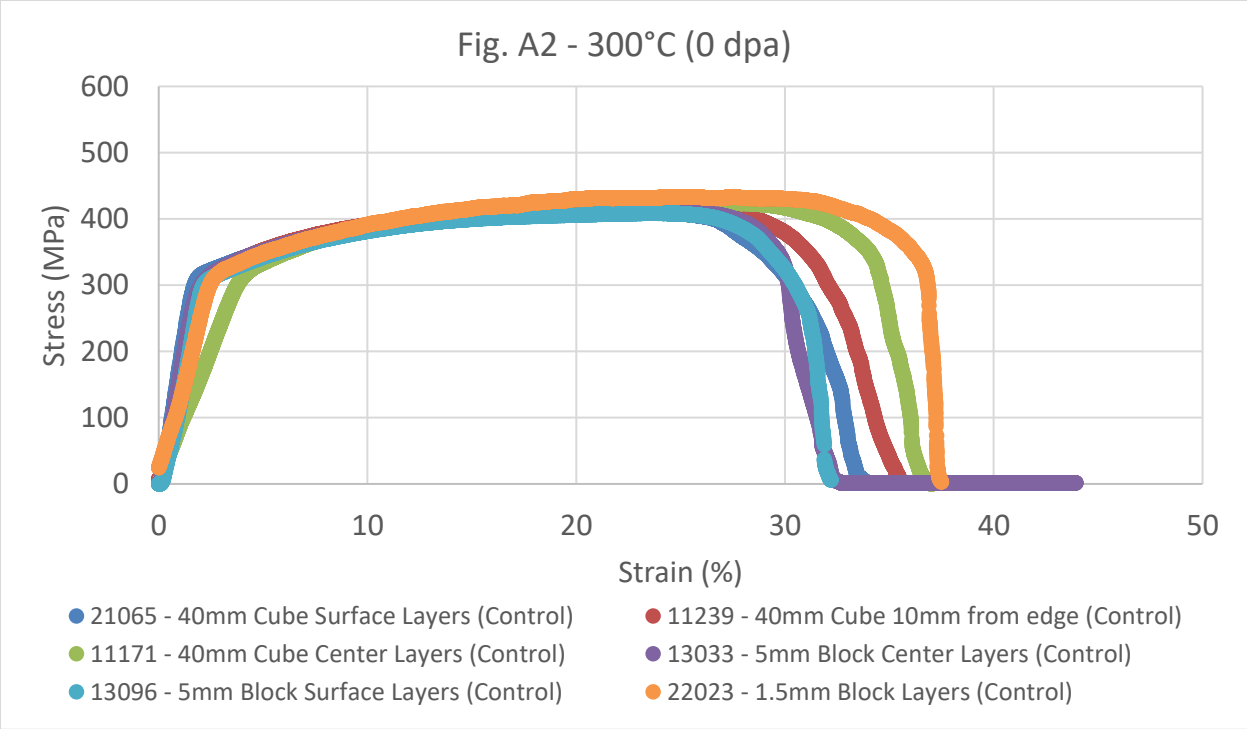
Fig. A2 - 300°C (0 dpa)
600
500
400
300
200
100
0
Stress (MPa)
0
10
20
30
40
50
Strain (%)
21065 - 40mm Cube Surface Layers (Control)
11239 - 40mm Cube 10mm from edge (Control)
11171 - 40mm Cube Center Layers (Control)
13033 - 5mm Block Center Layers (Control)
13096 - 5mm Block Surface Layers (Control)
22023 - 1.5mm Block Layers (Control)

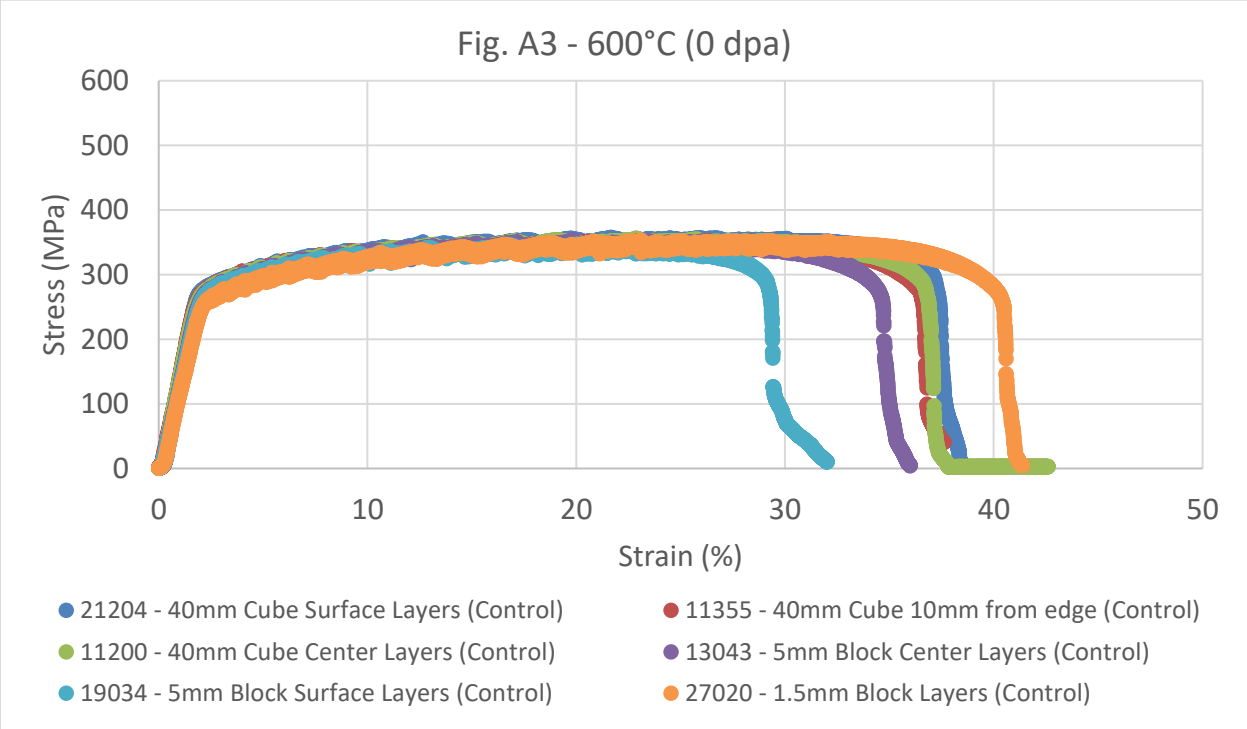
Fig. A3 - 600°C (0 dpa)
600
500
400
300
200
100
0
Stress (MPa)
0
10
20
30
40
50
Strain (%)
21204 - 40mm Cube Surface Layers (Control)
11355 - 40mm Cube 10mm from edge (Control)
11200 - 40mm Cube Center Layers (Control)
13043 - 5mm Block Center Layers (Control)
19034 - 5mm Block Surface Layers (Control)
27020 - 1.5mm Block Layers (Control)

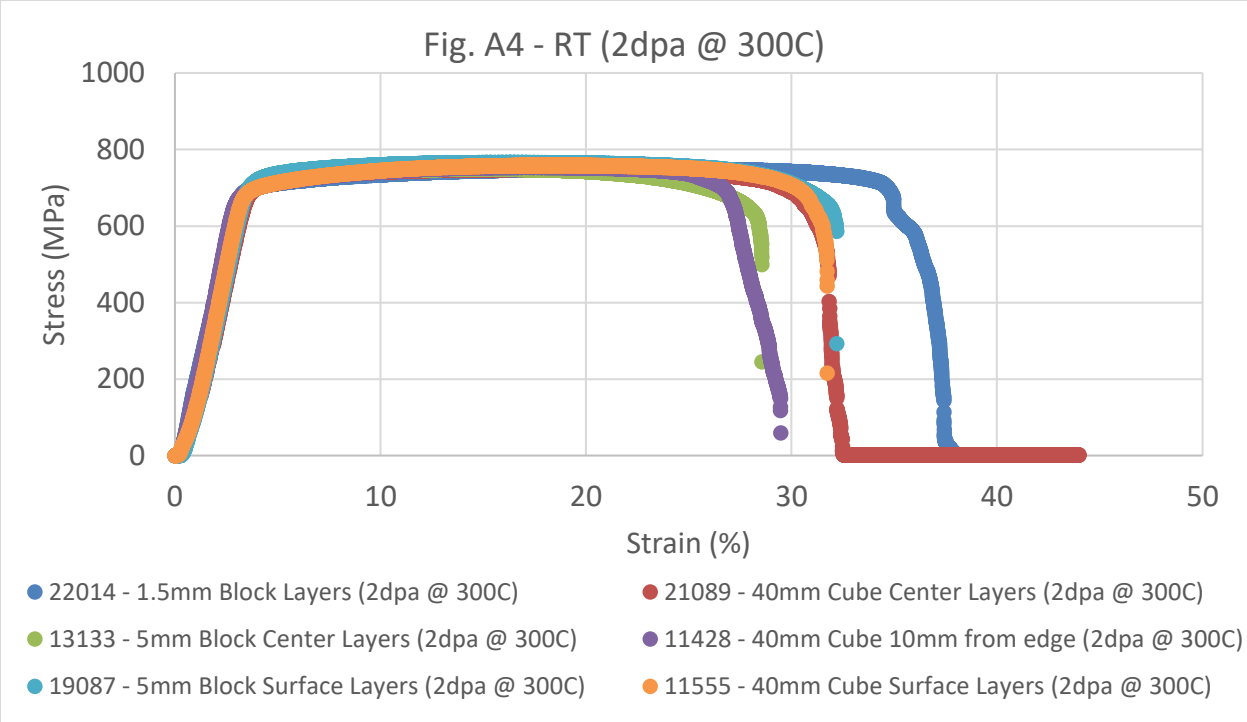
Fig. A4 - RT (2dpa @ 300C)
Stress (MPa)
1000
800
600
400
200
0
0
10
20
30
40
50
Strain (%)
22014 - 1.5mm Block Layers (2dpa @ 300C)
21089 - 40mm Cube Center Layers (2dpa @ 300C)
13133 - 5mm Block Center Layers (2dpa @ 300C)
11428 - 40mm Cube 10mm from edge (2dpa @ 300C)
19087 - 5mm Block Surface Layers (2dpa @ 300C)
11555 - 40mm Cube Surface Layers (2dpa @ 300C)

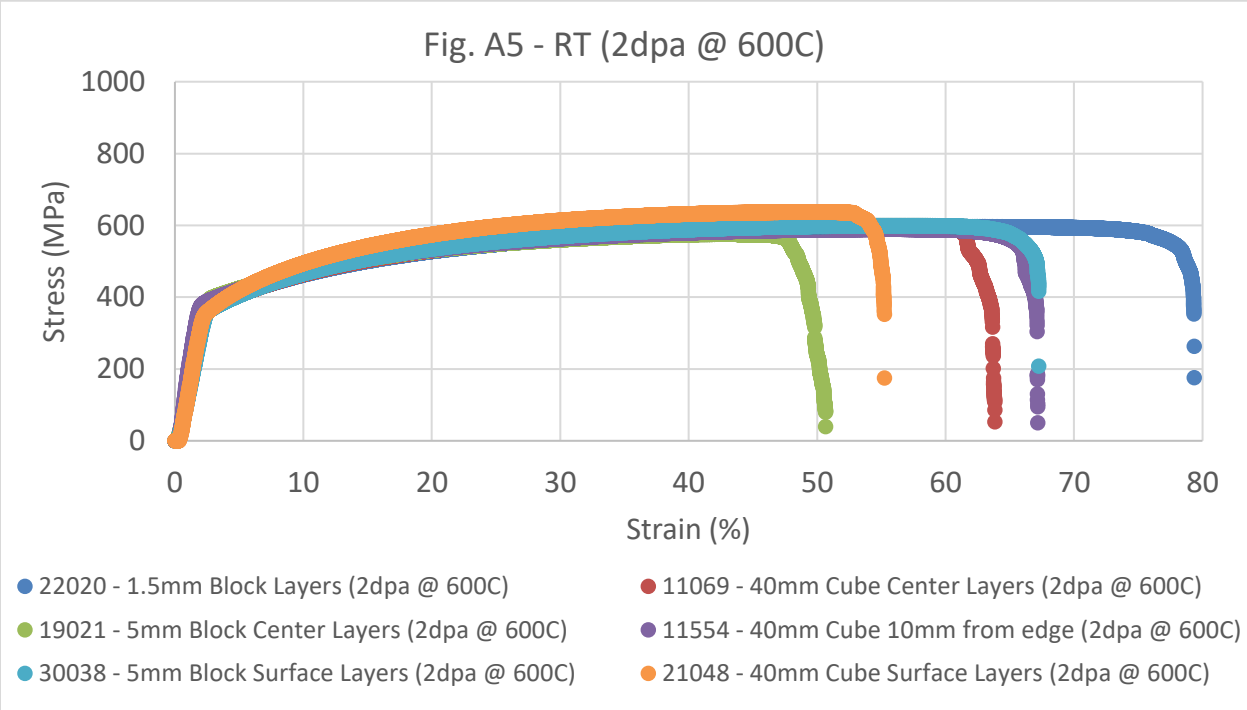
Fig. A5 - RT (2dpa @ 600C)
Stress (MPa)
1000
800
600
400
200
0
0
10
20
30
40
50
60
70
80
Strain (%)
22020 - 1.5mm Block Layers (2dpa @ 600C)
11069 - 40mm Cube Center Layers (2dpa @ 600C)
19021 - 5mm Block Center Layers (2dpa @ 600C)
11554 - 40mm Cube 10mm from edge (2dpa @ 600C)
30038 - 5mm Block Surface Layers (2dpa @ 600C)
21048 - 40mm Cube Surface Layers (2dpa @ 600C)

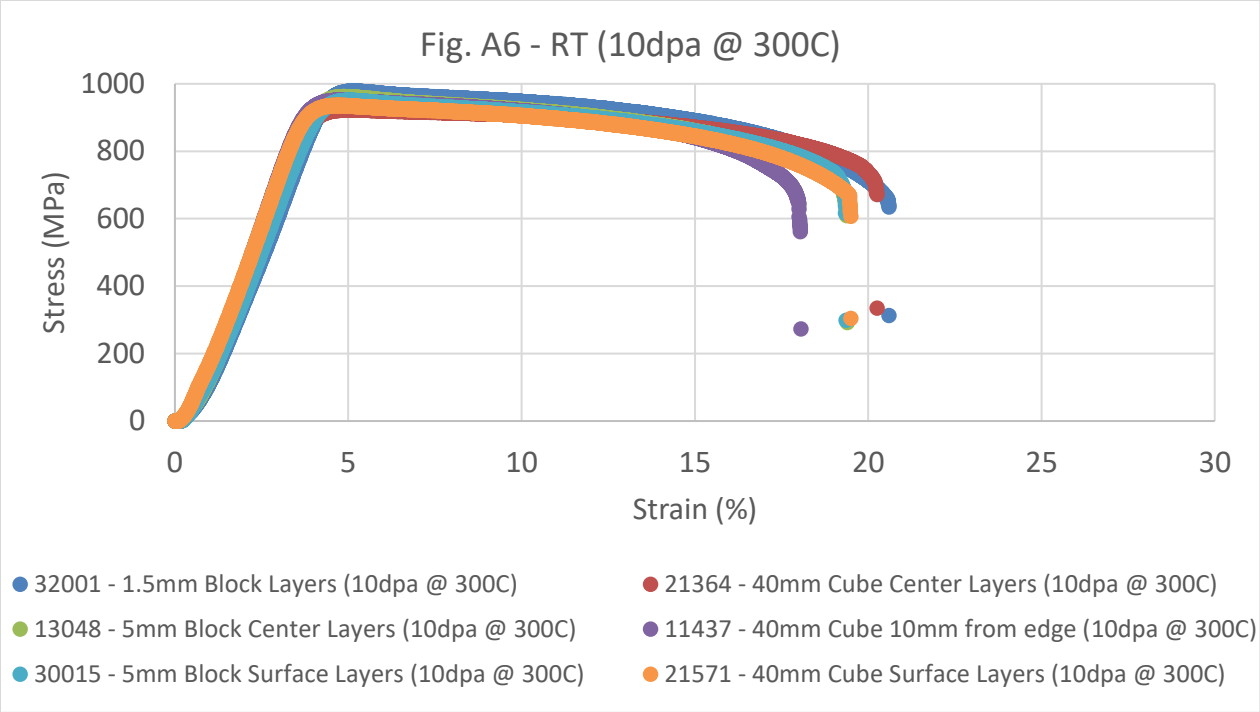
Fig. A6 - RT (10dpa @ 300C)
Stress (MPa)
1000
800
600
400
200
0
0
5
10
15
20
25
30
Strain (%)
32001 - 1.5mm Block Layers (10dpa @ 300C)
21364 - 40mm Cube Center Layers (10dpa @ 300C)
13048 - 5mm Block Center Layers (10dpa @ 300C)
11437 - 40mm Cube 10mm from edge (10dpa @ 300C)
30015 - 5mm Block Surface Layers (10dpa @ 300C)
21571 - 40mm Cube Surface Layers (10dpa @ 300C)

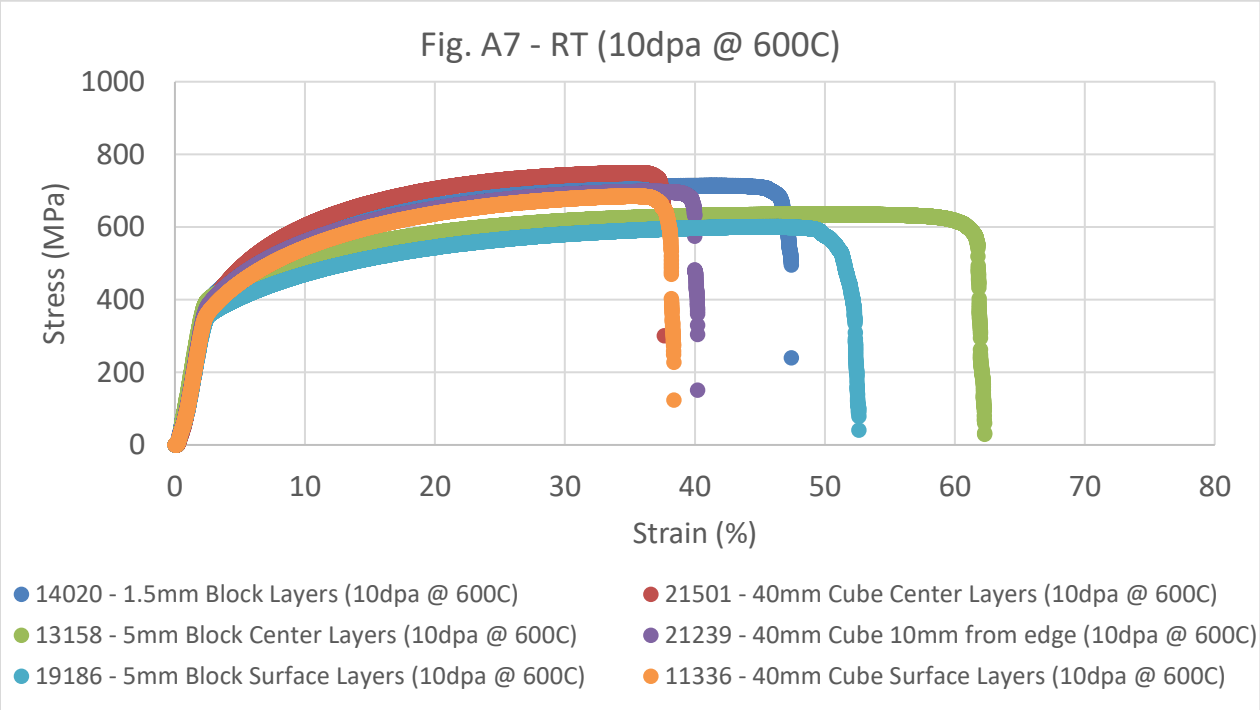
Fig. A7 - RT (10dpa @ 600C)
Stress (MPa)
1000
800
600
400
200
0
0
10
20
30
40
50
60
70
80
Strain (%)
14020 - 1.5mm Block Layers (10dpa @ 600C)
21501 - 40mm Cube Center Layers (10dpa @ 600C)
13158 - 5mm Block Center Layers (10dpa @ 600C)
21239 - 40mm Cube 10mm from edge (10dpa @ 600C)
19186 - 5mm Block Surface Layers (10dpa @ 600C)
11336 - 40mm Cube Surface Layers (10dpa @ 600C)

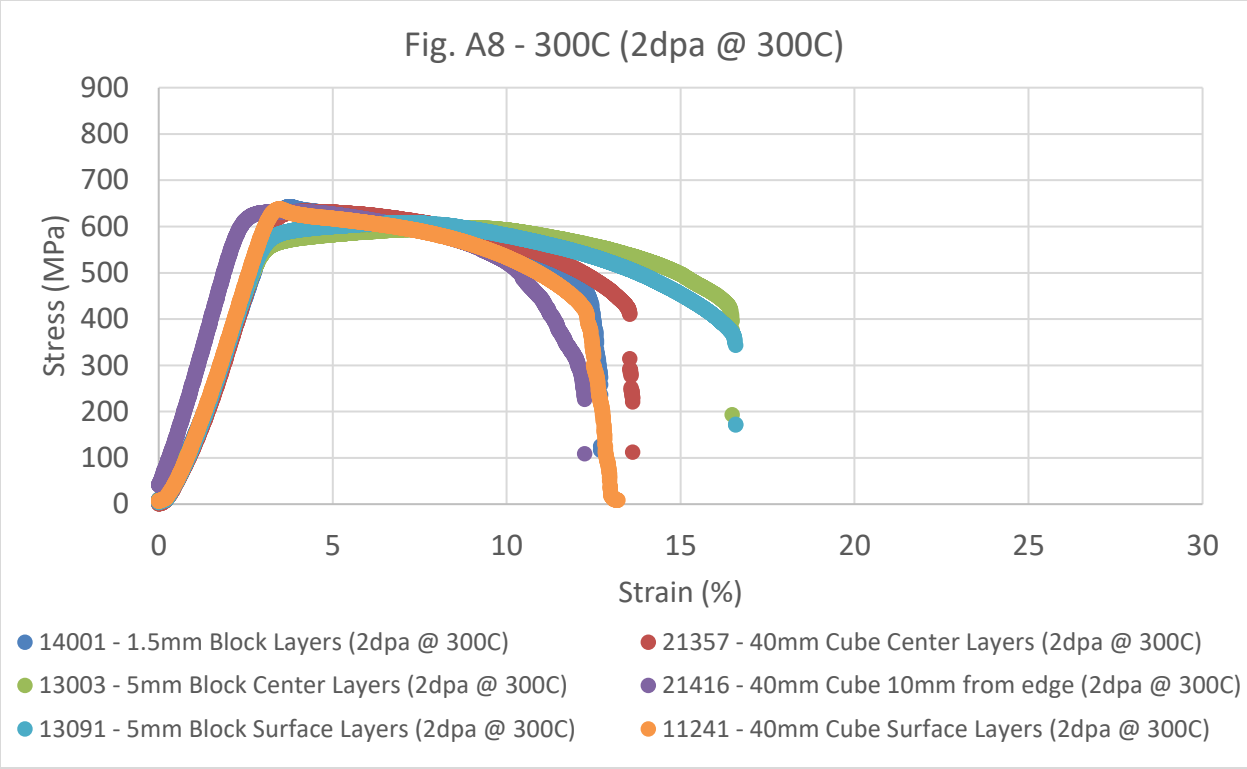
Fig. A8 - 300C (2dpa @ 300C)
Stress (MPa)
900
800
700
600
500
400
300
200
100
0
0
5
10
15
20
25
30
Strain (%)
14001 - 1.5mm Block Layers (2dpa @ 300C)
21357 - 40mm Cube Center Layers (2dpa @ 300C)
13003 - 5mm Block Center Layers (2dpa @ 300C)
21416 - 40mm Cube 10mm from edge (2dpa @ 300C)
13091 - 5mm Block Surface Layers (2dpa @ 300C)
11241 - 40mm Cube Surface Layers (2dpa @ 300C)

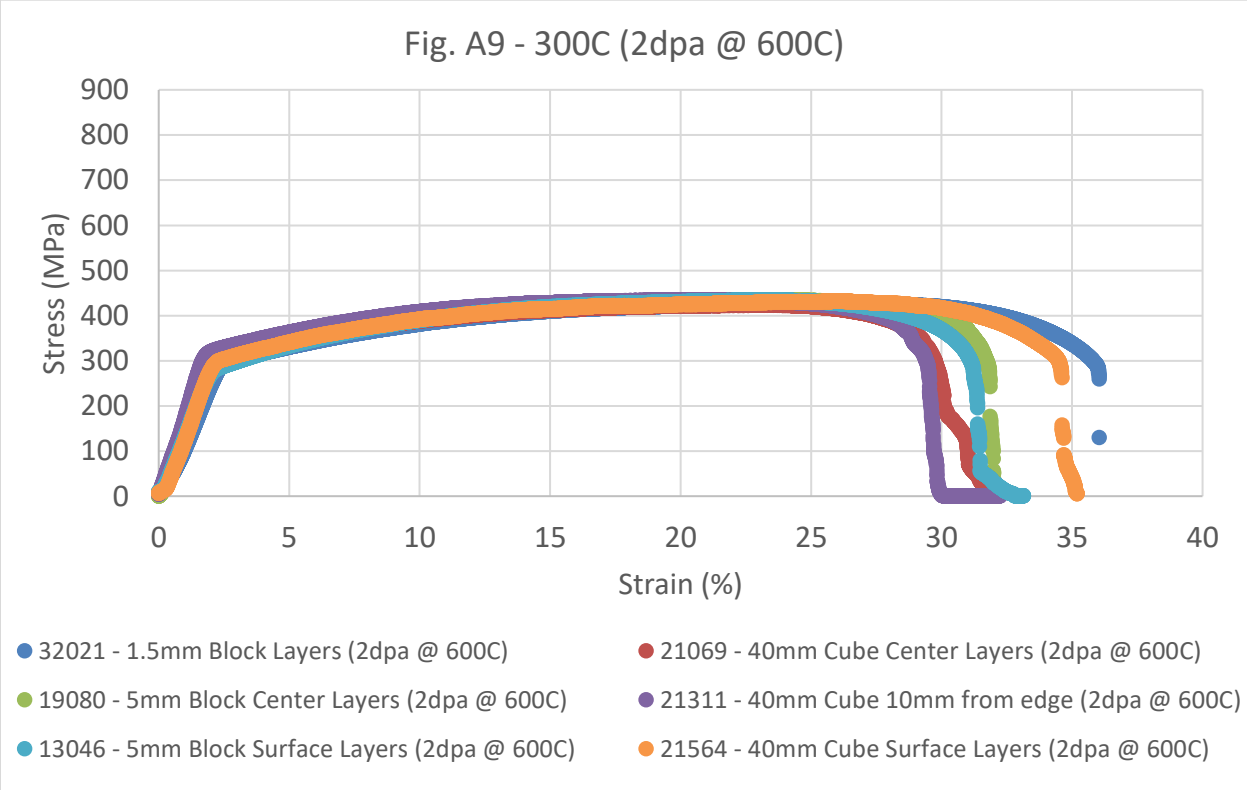
Fig. A9 - 300C (2dpa @ 600C)
Stress (MPa)
900
800
700
600
500
400
300
200
100
0
0
5
10
15
20
25
30
35
40
Strain (%)
32021 - 1.5mm Block Layers (2dpa @ 600C)
21069 - 40mm Cube Center Layers (2dpa @ 600C)
19080 - 5mm Block Center Layers (2dpa @ 600C)
21311 - 40mm Cube 10mm from edge (2dpa @ 600C)
13046 - 5mm Block Surface Layers (2dpa @ 600C)
21564 - 40mm Cube Surface Layers (2dpa @ 600C)

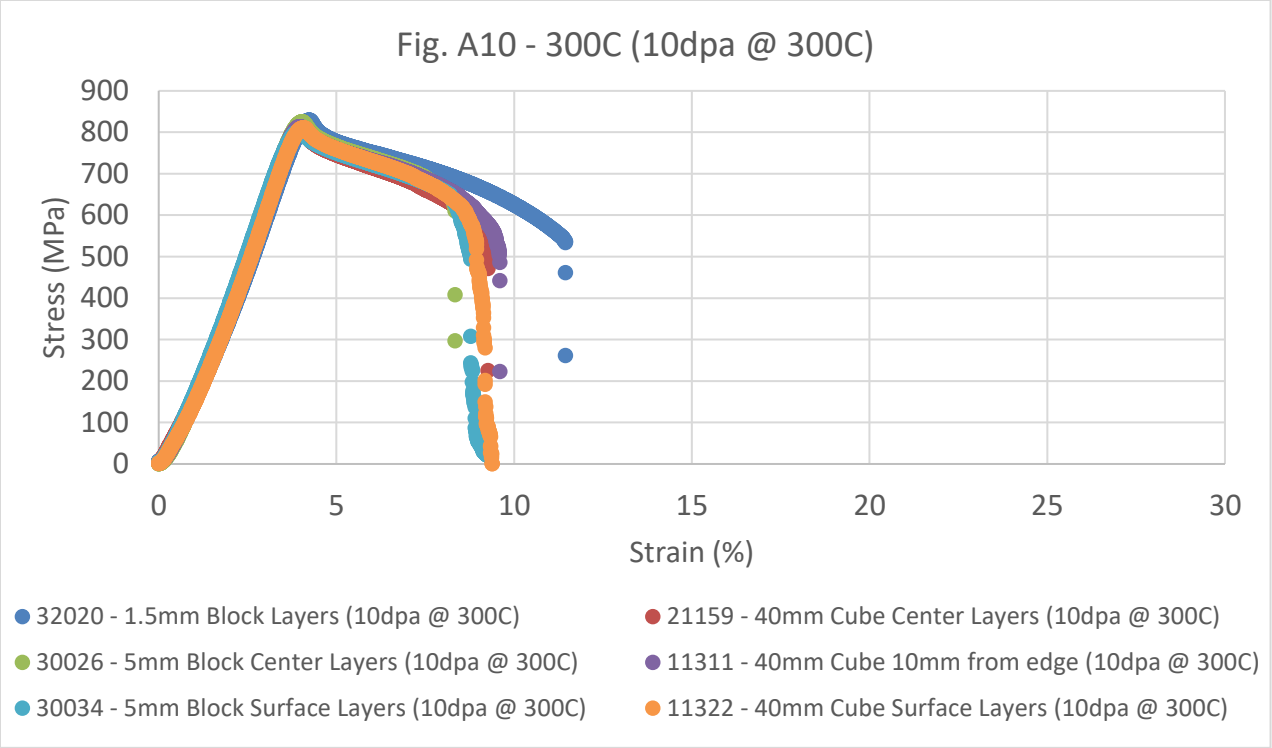
Fig. A10 - 300C (10dpa @ 300C)
Stress (MPa)
900
800
700
600
500
400
300
200
100
0
0
5
10
15
20
25
30
Strain (%)
32020 - 1.5mm Block Layers (10dpa @ 300C)
21159 - 40mm Cube Center Layers (10dpa @ 300C)
30026 - 5mm Block Center Layers (10dpa @ 300C)
11311 - 40mm Cube 10mm from edge (10dpa @ 300C)
30034 - 5mm Block Surface Layers (10dpa @ 300C)
11322 - 40mm Cube Surface Layers (10dpa @ 300C)

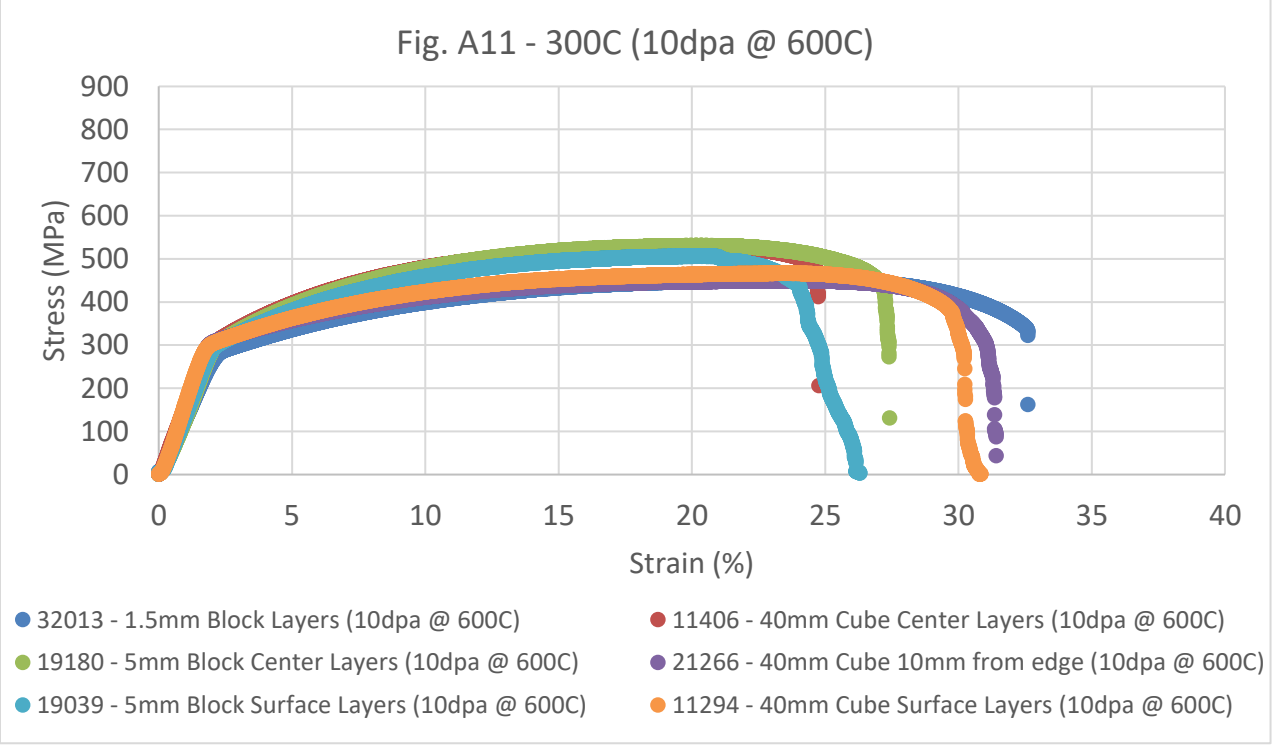
Fig. A11 - 300C (10dpa @ 600C)
Stress (MPa)
900
800
700
600
500
400
300
200
100
0
0
5
10
15
20
25
30
35
40
Strain (%)
32013 - 1.5mm Block Layers (10dpa @ 600C)
11406 - 40mm Cube Center Layers (10dpa @ 600C)
19180 - 5mm Block Center Layers (10dpa @ 600C)
21266 - 40mm Cube 10mm from edge (10dpa @ 600C)
19039 - 5mm Block Surface Layers (10dpa @ 600C)
11294 - 40mm Cube Surface Layers (10dpa @ 600C)

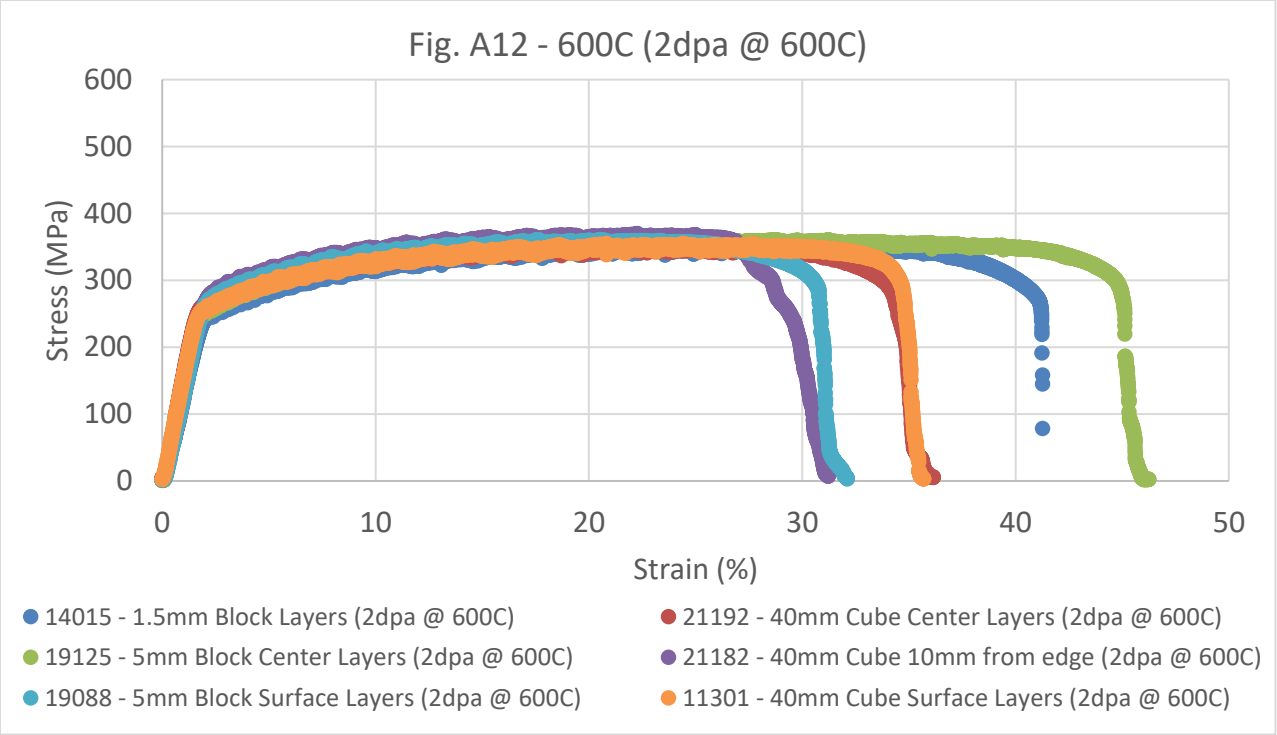
Fig. A12 - 600C (2dpa @ 600C)
Stress (MPa)
600
500
400
300
200
100
0
0
10
20
30
40
50
Strain (%)
14015 - 1.5mm Block Layers (2dpa @ 600C)
21192 - 40mm Cube Center Layers (2dpa @ 600C)
19125 - 5mm Block Center Layers (2dpa @ 600C)
21182 - 40mm Cube 10mm from edge (2dpa @ 600C)
19088 - 5mm Block Surface Layers (2dpa @ 600C)
11301 - 40mm Cube Surface Layers (2dpa @ 600C)

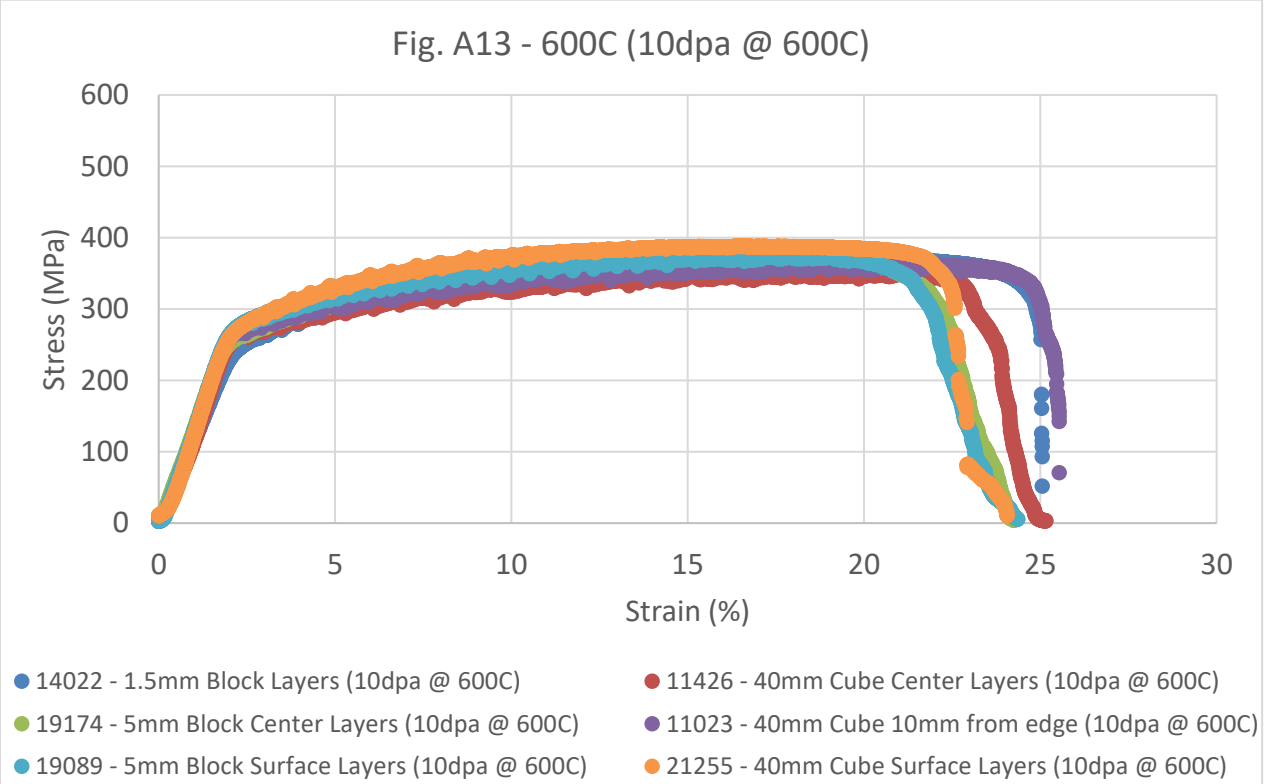
Fig. A13 - 600C (10dpa @ 600C)
Stress (MPa)
600
500
400
300
200
100
0
0
5
10
15
20
25
30
Strain (%)
14022 - 1.5mm Block Layers (10dpa @ 600C)
11426 - 40mm Cube Center Layers (10dpa @ 600C)
19174 - 5mm Block Center Layers (10dpa @ 600C)
11023 - 40mm Cube 10mm from edge (10dpa @ 600C)
19089 - 5mm Block Surface Layers (10dpa @ 600C)
21255 - 40mm Cube Surface Layers (10dpa @ 600C)